2010

Parameter Estimation In Heat Transfer And Elasticity Using Trained Pod-rbf Network Inverse Methods

Craig Rogers
University of Central Florida

University of
Central
Florida

STARS
Showcase of Text, Archives, Research & Scholarship

PARAMETER ESTIMATION IN HEAT TRANSFER AND ELASTICITY USING TRAINED
POD-RBF NETWORK INVERSE METHODS

by

CRAIG ALLAN ROGERS
B.S.M.E. University of Central Florida, 2008

A thesis submitted in partial fulfillment of the requirements
for the degree of Master of Science in Mechanical Engineering
in the Department of Mechanical, Materials and Aerospace Engineering
in the College of Engineering and Computer Science
at the University of Central Florida
Orlando, Florida

Summer Term
2010

ABSTRACT

In applied mechanics it is always necessary to understand the fundamental properties of a system in order to generate an accurate numerical model or to predict future operating conditions. These fundamental properties include, but are not limited to, the material parameters of a specimen, the boundary conditions inside of a system, or essential dimensional characteristics that define the system or body. However in certain instances there may be little to no knowledge about the systems conditions or properties; as a result the problem cannot be modeled accurately using standard numerical methods. Consequently, it is critical to define an approach that is capable of identifying such characteristics of the problem at hand. In this thesis, an inverse approach is formulated using proper orthogonal decomposition (POD) with an accompanying radial basis function (RBF) network to estimate the current material parameters of a specimen with little prior knowledge of the system. Specifically conductive heat transfer and linear elasticity problems are developed in this thesis and modeled with a corresponding finite element (FEM) or boundary element (BEM) method. In order to create the truncated POD-RBF network to be utilized in the inverse approach, a series of direct FEM or BEM solutions are used to generate a statistical data set of temperatures or deformations in the system or body, each having a set of various material parameters. The data set is then transformed via POD to generate an orthonormal basis to accurately solve for the desired material characteristics using the Levenberg-Marquardt (LM) algorithm. For now, the LM algorithm can be simply defined as a direct relation to the minimization of the Euclidean norm of the objective Least Squares function(s).

The trained POD-RBF inverse technique outlined in this thesis provides a flexible by which this inverse approach can be implemented into various fields of engineering and mechanics. More importantly this approach is designed to offer an inexpensive way to accurately estimate material characteristics or properties using nondestructive techniques. While the POD-RBF inverse approach outlined in this thesis focuses primarily in application to conduction heat transfer, elasticity, and fracture mechanics, this technique is designed to be directly applicable to other realistic conditions and/or industries.

This thesis is dedicated to Rick, Jill, Austin, Kindra, Rocco, Tyler, Katie and Mila. You've all made a huge impact in my life. Thank you for all being a close part of my life through family and friendship.

ACKNOWLEDGMENTS

I would like to acknowledge the University of Central Florida and the College of Engineering and Computer Science for providing me the opportunity to attend graduate school at their prestigious college and university. Without the support granted to me from my advisors Dr. Kassab and Dr. Divo in the Computational Mechanics lab as well as from the College of Engineering and the Department of Mechanical, Materials and Aerospace Engineering through tuition waivers, educational employment and student support, this thesis would have never came about.

TABLE OF CONTENTS

LIST OF FIGURES

LIST OF TABLES

LIST OF ACRONYMS

u	Snapshot vector
p	Vector of parameters
U	Snapshot matrix, matrix of data
Γ	Domain
f	Arbitrary functions
M	Number of snapshots
N	Number of nodes
K	Truncation point
ϕ	Basis functions/vectors
A	Amplitudes matrix
ε	Error
I	Identity Matrix
C	Covariance matrix (modified)
Q	Covariance matrix
V	Eigenvectors of C
L	Eigenvectors of Q
Λ	Matrix of eigenvalues
λ	Eigenvalues
σ	Singular values
Σ	Matrix of singular values

S	Left singular vector matrix of SVD, Matrix of eigenvectors
D	Right singular vector matrix of SVD, Matrix of eigenvectors
E	Component matrices
B	Matrix of interpolation coefficients
F	Matrix of radial basis functions
$f(p)$	Hardy inverse multi quadric radial basis function
c	RBF smoothing constants
$^-$	Truncated matrix
Ψ	Nonlinear least squares equation
α	Regularization constants
$k(x,y)$	Thermal conductivity
$T(x,y)$	Temperature
E	Elastic Modulus
G	Shear Modulus
v	Poisson's ratio
POD	Proper orthogonal decomposition
PCA	Principal component analysis
KLD	Karhunen-Loéve decomposition
SVD	Singular value decomposition
LM	Levenberg-Marquardt
NLS	Nonlinear Least Squares

CHAPTER 1 – INTRODUCTION

The topic of proper orthogonal decomposition (POD) has been around for more than a century, as a means of optimally correlating data using lines and planes as developed by Pearson in 1901 [13]. However, its application to the field of inverse problems, and engineering as a whole, has only begun to unfold in the last few decades. From an engineering aspect, POD produces many essential qualities that make it a valuable technique to implement practically and continuously. First, POD generates a series of optimal basis functions that allow for the best approximation of the field under study based on orthogonal constraints. Moreover, this optimality allows for the truncation of excess error that lies within the data or solution of the problem. By removing excess error, an enormous reduction in the computational time is established with respect to direct solvers such as the finite element method (FEM) [2][7]. This reduction in computing time is created due to the truncation aspects of POD. Essentially, POD is removing unnecessary constraints, or degrees of freedom, that have little effect on the system as a whole.

In regard to inverse problems, POD possesses many of the ideal characteristics that inverse algorithms pursue; mainly, model reduction, error filtration and regularization capabilities [2][7][11]. By utilizing these ideologies, the method of POD can be applied to numerous engineering applications that may have been tedious or laborious to solve otherwise. As will be seen in this thesis, POD (and its underlying family) has a natural ability for parameter estimation based on its inverse characteristics. Accordingly, POD combined with a radial basis

function (RBF) interpolation network can accurately reproduce material properties, dimensional aspects or even boundary conditions as they apply to an experimental or numerical model. In fact, it is the direct purpose of this thesis to use a POD-RBF network to inversely approximate material constants and dimensional traits in various engineering applications.

As will be discussed in Chapter 2, the method of POD utilizes the eigenvalues of the system in order to truncate excess error and significantly reduce the size of the problem. However, the interpretation of the eigenvalues may have a suggestively different meaning in regard to the POD family. Specifically the POD family is an assortment of many external methods, namely principal component analysis (PCA), Karhunen-Loéve decomposition (KLD) and singular value decomposition (SVD) [2][4][7][10]. While these methods have different formulations, it will be shown that they all share the same optimal equivalency, despite their various internal meanings.

Chapter 3 will take the reign in establishing the POD methodology as it applies to an inverse technique. It will illustrate the introduction of the RBF interpolation network in order to reproduce the experimental or numerical data field as well as the desired parameter(s). Once established the POD-RBF network will be applied to various applications presented in Chapter 4. These applications include a variety of examples from heat conduction, elasticity and fracture mechanics.

CHAPTER 2 – BACKGROUND

The concept of proper orthogonal decomposition (POD) began over a century ago as a statistical tool developed by Pearson [13] in order to correlate unclear data using only spatial lines and planes. Since that time POD has been redeveloped under various names and in vastly different applications. Depending on how the input data is utilized POD is also similarly known as Karhunen-Loéve decomposition (KLD), principal component analysis (PCA) or singular value decomposition (SVD) [2][4][7][10]. Furthermore, these techniques have been implemented in applications from signal processing and control theory, human face recognition, data compression, parameter estimation and many others [2][7]. Over the past thirty years these techniques have been greatly implemented into the engineering fields. The first reported use of these techniques into modern engineering applications was in the disciplines of fluid mechanics or computational fluid dynamics (CFD) in order to generate reduced modeled simulations [9]. This would then allow for much faster computational times while maintaining overall accuracy due to the optimal *bases* of POD. These techniques would later be expanded into more engineering applications such as heat transfer and elasticity as will be outlined in this thesis.

2.1 - Proper Orthogonal Decomposition

To begin the topic of proper orthogonal decomposition (POD), one should imagine a collection of vectors inside a Cartesian coordinate system [9][20]. Shown in Figure 1, a set of

vectors are assumed to be correlated if they are parallel to one another. Likewise, the vectors are said to be uncorrelated if the vectors appear orthogonal (or perpendicular) to one another.
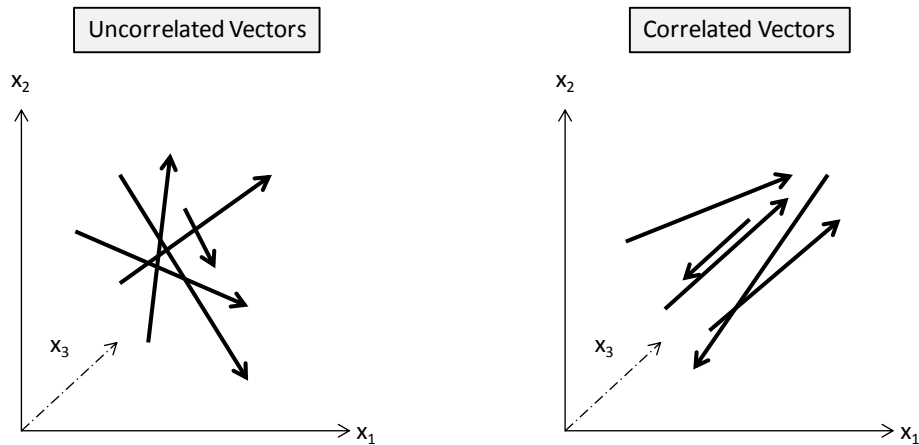
Figure 1 - Illustration of uncorrelated (left) and correlated (right) vectors

The primary goal of POD is to establish a rotated coordinate system using the smallest amount of coordinates needed [9]. For example, it may be possible to reduce the three dimensional Cartesian space into a two dimensional rotated coordinate frame if there is little variation in the third dimension. POD does this by capturing the maximum projections of the vectors (or data points) in the original frame. Accordingly, the first axis in the rotated POD frame captures the maximum projection of the vectors. This may commonly be referred to as the first *principal component* [16] (which will be defined further in section 2.1.1). The second axis in the POD frame, called the second principal component, captures the next orthogonal direction with the largest projection and so on. The rotated frame is illustrated in Figure 2.
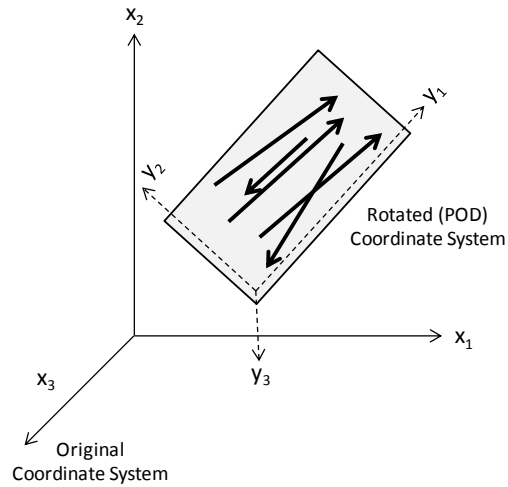
Figure 2 - Comparison of original and rotated (POD) coordinate system

The term *projection* is used loosely here since it may have some statistical, numerical or even physical meaning yet to be described. Nevertheless it is important to note that the variations of the projections diminish with respect to the new POD coordinate system. For instance, the first axis will hold the largest projection, the second axis will hold the next largest projection and the third axis (if there is one) will hold the third largest projection. Utilizing this feature allows POD to give a better approximation of the higher correlated (parallel) vectors with fewer coordinates (or components).
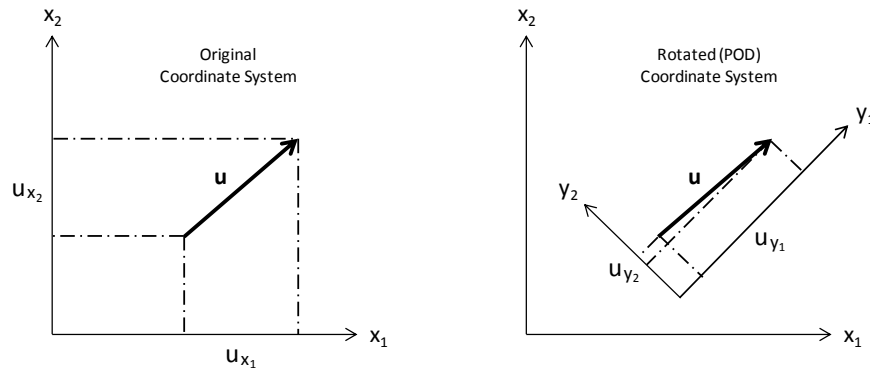
Figure 3 - Approximation of a Vector in the Original (left) and POD (right) Coordinate Frame

It can be seen in Figure 3, that it would take two coordinates of the original frame to approximate a vector **u** accurately. However in the POD rotated configuration, one coordinate could produce an excellent approximation since there is little variation in the second coordinate. In an ideal scenario POD can represent all vectors using only one coordinate axis, as seen in Figure 4 (right). On the other hand, POD may have to use many coordinate axes to produce an accurate depiction of the data as shown in Figure 4 (left). However, it should be noted that Figure 4 (left) and Figure 4 (right) represent extreme cases of data collection [16]. Typical data would fall into a variation of Figure 4 (middle).
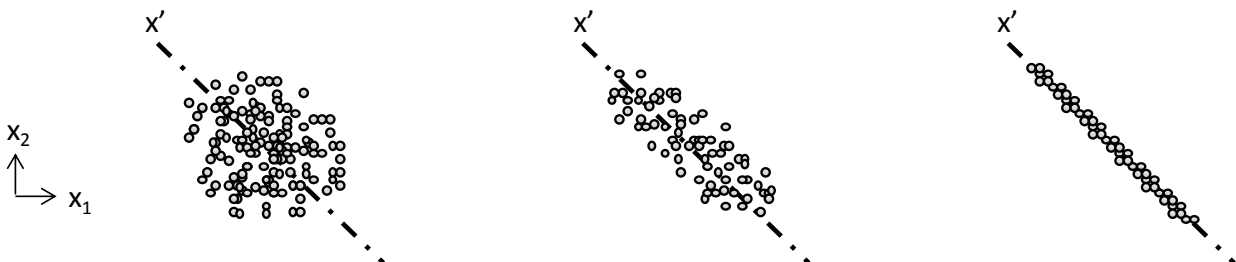
Figure 4 - Various Data Representations. Highly Uncorrelated Data (left), Correlated Data (middle), Highly Correlated Data (right).

6

To put a mathematical interpretation to POD, one can imagine the approximation of a continuous function that exists within a known domain Γ.

$$f(x) \approx \sum_{i=1}^{M} \phi_i A_i \qquad (1)$$

Of course ϕ can be chosen arbitrarily (or by a set of shape functions, etc…) such that as M approaches infinity, the approximation typically approaches exactness. However the best approximation is not always guaranteed. In POD the best approximation is guaranteed by using the least squares minimization of the L_2 norm [4][9][10].

$$\varepsilon = \left\| f(x) - \sum \phi A \right\| \qquad (2)$$

POD also establishes a set of orthogonality constraints for the selection of the basis functions ϕ. Where orthogonality states

$$\phi^T \phi = I \qquad (3)$$

which allows for the approximation of the amplitudes $\mathbf{A}$.

$$A = \phi^T f \qquad (4)$$

In a more general discrete case, a matrix $\mathbf{U}$ can be used to store previously known information of the problem. In a transient problem, the previously known information may refer to data attained during the first initial time steps [2][7]. The matrix $\mathbf{U}$ is called the snapshot matrix and can be defined as follows

$$U = \sum_{i=1}^{M} \phi^i A_i \qquad (5)$$

In matrix-vector notation (5) can be rewritten as

$$U = \phi A \qquad (6)$$

In our discrete case **U** and ϕ are rectangular matrices of dimensions $N \times M$ and **A** is a rectangular matrix of dimensions $M \times M$. Where M corresponds to the total number of snapshots and N represents the number of nodes used to approximate the system. The method of snapshots will be defined later in Chapter 3.

On the other hand, if only K terms are now used to approximate **U** whereby $K < M$, then the problem may be reduced (often times significantly) and look similar to the continuous case in (1).

$$U \approx \sum_{i=1}^{K} \phi^i A_i \qquad (7)$$

The selection of K can be chosen arbitrarily for a quick solution, although this is not ideal. In regards to the family of POD, the selection of K yields very important information regarding the internal structure of the data [10][16] and will be the discussion of the next few sections.

It may also serve to note that the basis vectors generated via POD may entail some sort of physical meaning. As will be shown in Chapter 4.1, the POD basis vectors possess a correlation to analytical eigenfunctions from Fourier analysis in heat transfer. In elasticity (and even vibration problems), the basis vectors may also be related to the modal shapes as well. Although elasticity examples are not shown in this thesis, the reader may refer to [21].

2.1.1 - Principal Component Analysis

Regarded as the oldest method in the POD family, principal component analysis (PCA) was developed as a statistical method by Pearson [13] and Hotelling in the early twentieth century [2][4]. Its purpose is to identify a hidden or unclear internal structure within a collection of multivariable stochastic data. Like POD, PCAs main objective is to reduce the dimensionality of the data. Typically the data set has a large number of interrelated variables which may be indistinguishable to a human eye. So in order to reduce the dimensionality PCAs goal is to maintain as much variation in the data as possible. To achieve this, PCA transforms the original variables into new variables called *principal components*. The principal components are entirely uncorrelated and ordered such that the first principal components have the most variation of the original variables. In POD, this would correspond to the optimal selection of coordinate axes to best fit the data. In PCA (or statistics in general), the variation is the measure of the variance σ^2 inside the data [16]. For a more applied sense, the variance is simply the eigenvalues of a modified covariance matrix of the data **U**. The modified covariance matrix **C** takes the form

$$C = U^T U \tag{8}$$

such that the variances (or eigenvalues) can be determined from the nontrivial solution of a standard eigenvalue problem.

$$CV = V\Lambda \tag{9}$$

The eigenvalues Λ and eigenvectors **V** can be determined via singular value decomposition (SVD) or eigenvalue decomposition. For the sake of later validity and common practice, SVD is used to estimate the eigenvalues and eigenvectors. The corresponding singular values correspond

to the standard deviations σ of the data set (where the variance is the square of the standard deviation).

$$\sigma_i = \sqrt{\lambda_i} \qquad (10)$$

Of course λ represents the eigenvalues. The optimal basis can be generated in PCA as

$$\phi = UV\Sigma^{-1} \qquad (11)$$

where Σ represents a diagonal matrix of singular values (or standard deviations) found in (10). For completeness a comparison of the PCA to SVD [9][10] is shown in the Appendix.

The next important step in PCA (and POD methods in general) is the truncation process. The truncation procedure is commonly referred to as model reduction because the main goal is to reduce the total number of degrees of freedom inside the system. To do so in PCA, one must look at the variances occurring at each principal component. The variances will decrease in a rapid sense from a large initial variance (first principal component) to a small variance that remains relatively constant through the remainder of the data set. The truncation of the variances can then occur when there is little change in the variation, as shown in Figure 5.
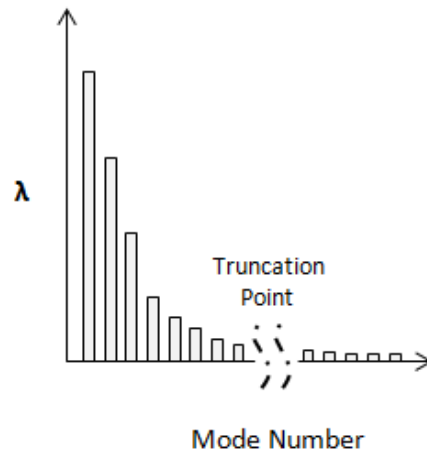
Figure 5 - Truncation of Eigenvalues for Model Reduction

10

As will be later noted in Chapter 4, the truncation process can significantly reduce the size of the problem while maintaining a large level of accuracy in the estimation of the solution. While some authors [16][17] denote a specific point (or equation) at which the truncation of data begins to severely affect the error of the estimation, a good rule to follow is to truncate the eigenvalues once they get below a minimum value or begin to remain constant in value.

2.1.2 - Karhunen-Loéve Decomposition

Another aforementioned member in the family of POD is called Karhunen-Loéve decomposition (KLD). Although the name refers to both Karhunen and Loéve, the method was independently developed by Karhunen in the 1940's and further expanded upon by Loéve in later years [4][10]. KLD represents a theory regarding optimal series expansion of continuous stochastic processes. This can also be seen as an extension of PCA to infinite dimensional spaces; however, in a discrete sense KLD has the same optimal properties as variance maximization in PCA [10]. The primary difference of KLD is that it measures the mean square error that is generated after reducing the dimensionality.

The concept of KLD can be developed from [9][10] which utilizes the covariance of the matrix **U**.

$$Q = UU^T \tag{12}$$

It should be noted that in PCA a modified covariance matrix **C** is used (the benefits of each covariance matrix will be touched upon later in this section). Analogous to PCA, KLD will use

the nontrivial solution to the eigenvalue problem to determine the eigenvalues Λ and eigenvectors **L** of the covariance matrix **Q**.

$$QL = L\Lambda \tag{13}$$

The eigenvectors **L** in KLD and the eigenvectors **V** in PCA are not equivalent as a result of the choice of covariance matrices used in each method. However, once the eigenvectors and eigenvalues are calculated, the selection of the basis functions can then be chosen. In KLD the basis functions can be written as

$$\phi = L \tag{14}$$

This states that the basis functions ϕ are equivalent to the KLD eigenvectors **L**. In turn, the selection of the KLD eigenvectors as the basis functions can be proven to be a good choice, since the basis functions in both KLD and PCA are identical despite the different derivations. This also relates to the equivalency of the POD methods (which is shown in detail in the Appendix).

The eigenvalues λ now represent the error produced from the KLD approximation. While the main goal of KLD is to minimize the mean square error [10], its goal as a member of POD is to create a reduced order model for approximation while maintaining overall accuracy. By observing the error (and as a result the eigenvalues), a point K can be chosen so the error remains at a suitable minimal value. The mean square error is denoted as the summation of the eigenvalues with respect to the truncation point K.

$$\varepsilon^2 = \sum_{i=k+1}^{M} \lambda_i \tag{15}$$

Notably the first eigenvalues represent the most information (and have higher values) which would dramatically increase the error if the process was truncated early. So as the eigenvalues begin to achieve constancy, as in Figure 5, the truncation process can then occur.

For earlier clarity, one may take into account the choice of the covariance matrices used in PCA and KLD for computational considerations [9]. Specifically, the covariance matrix $\mathbf{C}$ in PCA is of size $M \times M$, while the covariance matrix $\mathbf{Q}$ in KLD is of size $N \times N$. In large examples where the number of nodes N is much greater than the number of snapshots M ($N \gg M$), the method of KLD will prove to be more time consuming as a result of the covariance matrix selection. In this situation, the method of PCA may yield much faster results (which is the primary goal of model reduction techniques). In regards to this thesis, the size of $\mathbf{U}$ is relatively equivalent on each dimension so the choice of each method yields similar computational times and will not be further discussed.

2.1.3 - Singular Value Decomposition

Unlike the other POD methods stated above, the singular value decomposition (SVD) approach does not present a suitable physical meaning to the data. In the logic of POD, the eigenvalues represent the energy present within the system (or the amount of information each principal component holds). The eigenvalues in PCA and KLD represent the variances [16] and errors [10], respectively. Nevertheless SVD is still directly comparable to POD because it finds the same essential characteristics that operate under POD, the eigenvalues and eigenvectors.

While a true (in depth) derivation of SVD can be found within many references [10][14][19], a short overview in regards to POD will be given here from [9].

Our matrix of data $\mathbf{U}$ can be broken into SVD components, as shown in (16).

$$U = S\Sigma D^T \qquad (16)$$

Where $\mathbf{S}$ and $\mathbf{D}$ represent the left and right singular vector matrix of $\mathbf{U}$ respectively and Σ denotes a matrix of singular values σ_i arranged in descending order ($\sigma_1 > \sigma_2 > \cdots > \sigma_r$). Furthermore, if the matrix $\mathbf{U}$ is real, the matrices $\mathbf{S}$ and $\mathbf{D}$ are always orthogonal (or $\mathbf{S^T S} = \mathbf{I}$ and $\mathbf{D^T D} = \mathbf{I}$ where $\mathbf{I}$ is the identity matrix). $\mathbf{U}$ can now be decomposed into a series of additive component matrices

$$U = E_1 + E_2 + \cdots + E_r \qquad (17)$$

where r represents the minimum dimension of the matrix $\mathbf{U}$ ($N \times M$). Equating the above equations yields

$$E_i = S^i \Sigma^i_i D_i^T \qquad (18)$$

where the upper and lower indices in (18) represent the corresponding i^{th} column and row vector respectively. The component matrices $\mathbf{E}$ are also known to be orthogonal to one another. Now the singular values σ can be extracted using the norm of the component matrices

$$\left\| E_i \right\| = \sigma_i \qquad (19)$$

which are the diagonal terms stored in Σ. Like the other POD methods $\mathbf{E}_i$ can be considered as the critical components of $\mathbf{U}$ (or the principal components). As stated above, the singular values are stored in descending order. This now provides insight to the contribution of each component matrix $\mathbf{E}_i$ because the largest singular value corresponds to the greatest contribution (or

knowledge) to the data matrix $\mathbf{U}$. This result can then be substituted into the general POD approximation (6) which yields

$$E_i = \phi^i A_i \tag{20}$$

Comparing (18) and (20) it can be denoted that the left singular vector matrix $\mathbf{S}$ corresponds to the orthogonal basis functions ϕ.

$$\phi = S \tag{21}$$

This also means that the left singular vector matrix corresponds to the eigenvectors (as already known through references of SVD).

Like the other POD methods, the truncation point can be determined by observing the rapid decrease in the eigenvalues as shown in Figure 5.

<u>2.2 - Inverse Methods</u>

The idea of inverse algorithms has been studied for decades, ever since the mainstream use of numerical methods began to emerge. Different concepts have been outlined by many authors [14] with techniques to retrieve the best solution. The main technique developed for solving inverse problems is primarily regularization; however, other methods like model reduction and/or error filtration also benefit the inverse approximation.

The application of POD as an inverse method arose due to the demanding task of solving an ill-posed inverse problem. POD is utilized by finding the correlation between the known direct problem and the solution to be desired [11]. Moreover, POD is utilized to produce a low-order but high quality approximation of the solution field. As stated previously, POD is capable

of capturing dominant components of the data with typically only a few modes or degrees of freedom. This is due to the ability of POD to approximate a set of vectors using an optimal rotated coordinate frame [9][11][16].

Of course, the primary reason POD is favorable in solving inverse problems is that it provides many of the desired characteristics for solving inverse problems. These ideal attributes include model reduction, error filtration and regularization.

CHAPTER 3 – METHODOLOGY

The first step in the implementation of POD is the creation of the *snapshot* which is the collection of N sampled values of **u** of the field under consideration [2][7][11]. In the case of this thesis the sampled fields recorded represent the temperatures or deformations within a body or system. Accordingly each snapshot is stored in a vector **u**. A collection of M snapshots denoted as $\mathbf{u}^j$ (for $j = 1, 2 \ldots M)$ are then generated by altering the parameter(s) **p** upon which the field depends on. In the current scope of this thesis, the altered parameters are essentially material properties but can likewise be a combination of material properties, boundary conditions or dimensional characteristics. Each $\mathbf{u}^j$ is then stored inside rectangular $N \times M$ matrix **U** denoted as the snapshot matrix (with N corresponding to the number of sampled nodes or locations). The concept of the snapshot can be seen in Figure 6.
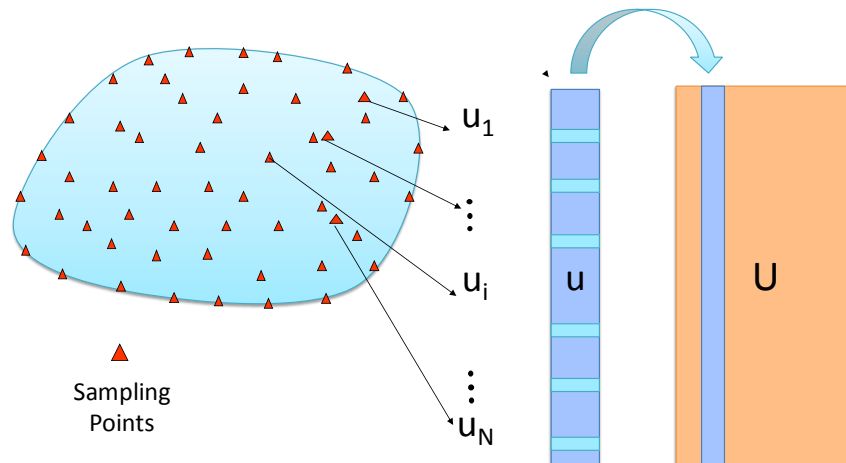
Figure 6 - Illustration of a snapshot of the data field

The snapshot field may be created by numerical modeling of the system, say FEM or BEM, or from actual empirical data. The goal of POD is to establish a set of orthonormal vectors ϕ^j resembling the snapshot matrix $\mathbf{U}$ in an optimal way [11]. The matrix ϕ is commonly referred to as the POD *basis* and can be seen in (22).

$$\phi = U \cdot V \tag{22}$$

As denoted in Chapter 2, $\mathbf{V}$ represents the eigenvectors of the covariance matrix $\mathbf{C}$ and can easily be derived using the nontrivial solution of the general eigenvalue problem denoted in (9). It may also serve to note that the covariance matrix $\mathbf{C}$ is symmetric and positive definite and the eigenvalues λ are always real and positive. Typically at this time the eigenvalues are sorted in descending order and can be directly attributed to the energy of the system. This energy decreases rapidly with the increasing mode number as illustrated in Figure 5. This allows the user to neglect majority of the modes of lower value since they hold little energy (or information) within the system. As stated throughout Chapter 2, this is referred to as the truncation of the POD basis and is accomplished by deciding which fraction energy inside the system should be removed for later calculations. The resulting POD basis $\bar{\phi}$ referred to as the *truncated* POD basis consists of $K < M$ vectors such that

$$\bar{\phi} = U \cdot \bar{V} \tag{23}$$

Which corresponds to the truncation of the eigenvector matrix denoted as $\bar{V}$. This also stores the first K eigenvectors of the covariance matrix. The truncated POD basis in (23) is also orthogonal and presents optimal approximation properties as described in Chapter 2. Once $\bar{\phi}$ is known, the snapshot matrix $\mathbf{U}$ can be regenerated using

$$U = \bar{\phi} \cdot A \tag{24}$$

A stands for the amplitude's associated with $\mathbf{u}^j$. Referring to the orthogonality of the basis functions, the amplitude's can be determined from

$$A = \bar{\phi}^T \cdot U \tag{25}$$

At this time the data may begin to be extrapolated for information on the current problem. To do this, consider a vector **p** which stores the necessary parameters on which the solution depends. In the current scope only one parameter is to be considered; however, in the presence of a transient problem other parameters may be stored, such as time and other properties. The transient derivation is not described in this thesis, for more information refer to [2][7][12].

The amplitudes **A** are defined as a nonlinear interpolation function of the parameter vector **p** described in (27). Of course, the amplitudes **A** can be related to the interpolation functions by an unknown matrix of constant coefficients **B**.

$$A = B \cdot F \tag{26}$$

F is defined as the matrix of interpolation functions, where the set of interpolation functions $f_i(\mathbf{p})$ can be chosen arbitrarily. However, some choices of interpolation functions may lead to an ill-conditioned system of equations for the coefficient matrix **B**. In this analysis, radial basis functions (RBF) have been used as the interpolating function of choice due to their nice approximation and smoothing properties [11]. Here the Hardy inverse multi-quadric radial basis function has been employed and is defined as

$$f_i(p) = f_i\left(\left|p - p^i\right|\right) = \frac{1}{\sqrt{\left|p - p^i\right|^2 + c^2}} \tag{27}$$

where c is defined as the RBF smoothing factor and $\mathbf{p}^i$ corresponds to the same parameter $\mathbf{p}$ used to generate $\mathbf{u}^i$ (for $i = 1, 2 \dots M$). It should be seen that the argument of the ith RBF is the distance $|\mathbf{p} - \mathbf{p}^i|$ or the distance between its current parameter $\mathbf{p}$ and the reference parameter $\mathbf{p}^i$ [11].

To use (26), the matrix of coefficients $\mathbf{B}$ needs to be evaluated, which can be done by simple inversion methods.

$$B = A \cdot F^{-1} \tag{28}$$

As stated, $\mathbf{F}$ is the matrix of interpolation functions defined as a set of M vectors $f(\mathbf{p})$, which can be visualized as

$$F = \begin{bmatrix} f_1(|p^1 - p^1|) & \cdots & f_1(|p^j - p^1|) & \cdots & f_1(|p^M - p^1|) \\ \vdots & & \vdots & & \vdots \\ f_i(|p^1 - p^i|) & \cdots & f_i(|p^j - p^i|) & \cdots & f_i(|p^M - p^i|) \\ \vdots & & \vdots & & \vdots \\ f_M(|p^1 - p^M|) & \cdots & f_M(|p^j - p^M|) & \cdots & f_M(|p^M - p^M|) \end{bmatrix} \tag{29}$$

where $\mathbf{p}^i$ and $\mathbf{p}^j$ are used to generate i^{th} or j^{th} snapshot respectively. This is commonly referred to as collocation.

At this point it should be emphasized that the matrix of amplitudes $\mathbf{A}$ and the matrix of coefficients $\mathbf{B}$ are known using the above relations. Now equating (25) and (26) yields the following

$$\bar{\phi}^T \cdot U = B \cdot F \tag{30}$$

Using the orthogonality of $\bar{\phi}$ it can easily be seen that the snapshot matrix $\mathbf{U}$ can be approximated as

$$U \approx \bar{\phi} \cdot B \cdot F \qquad (31)$$

Now a low dimensional truncated model of (24) can be seen in vector form as

$$u(p) \approx \bar{\phi} \cdot B \cdot f(p) \qquad (32)$$

This model will now be referred to as the *trained* POD-RBF network and is completely capable of reproducing the data field that correspond to any arbitrary set of parameters $\mathbf{p}$ within the initial snapshot domain [2][7][11]. Likewise, extrapolation outside the range of $\mathbf{p}$ used to generate the initial snapshots $\mathbf{u}^i$ can lead to poor accuracy and approximation of the model.

Finally, the trained POD-RBF network in (32) is used to retrieve the values of the unknown parameter vector $\mathbf{p}$ for the inverse method. This is done in a least squares sense by taking the sum of the squares of the data obtained from $\mathbf{u(p)}$ and subtracting it from the actual experimental (or numerical) data $\mathbf{y}$. It is typically best to use the same sensor points utilized in empirical data as the same nodal points, N, used in the numerical simulation as it leads to less interpolation and better overall accuracy; however, it is not necessary. In a general form, the nonlinear least squares equation is written as

$$\Psi = \sum_{i=1}^{N} \left(u(p)_i - y_i \right)^2 \qquad (33)$$

In the case of this thesis, the least squares equation is implemented using Levenberg-Marquardt (LM) to solve for the desired parameter $\mathbf{p}$. This generates what is known as the least squares objective function [14] and is shown in (34) with the addition of a regularization parameter α for further accuracy.

$$J(p) = \left[\sum_{i=1}^{N} \left(u_i(p) - y_i \right) \frac{\partial u_i(p)}{\partial p} \right] + \alpha \left[\sum_{i=1}^{N} \left(u_i(p) - \overline{y} \right) \frac{\partial u_i(p)}{\partial p} \right] \qquad (34)$$

(34) simply represents the partial derivative of (33) with respect to the unknown parameter **p** with $\overline{y}$ denoting the mean of **y**.

Now (34) can be solved using LM to estimate the unknown parameter **p**. Applications of this methodology are shown in Chapter 4 with examples ranging from basic conductive heat transfer to linear elastic fracture mechanics.

CHAPTER 4 – APPLICATIONS

A wide variety of applications in mechanics are used to demonstrate the robustness and importance of this POD-RBF technique to inverse methods. Specifically, applications will range from simple heat conduction problems to more comprehensive elasticity problems.

The first set of examples in Section 4.1 will outline basic heat conduction problems using simple domains in order to determine the spatially dependent thermal conductivity of an unknown material. Likewise, a more detailed two dimensional heat conduction problem using a complex domain will then be used to determine the thermal conductivity using noisy temperature distributions from random points within the body.

In Section 4.2, a series of elasticity problems will be modeled in order to accurately estimate the modulus of elasticity, the shear modulus and Poisson's ratio using only noisy deformation data. The first elasticity example will use a two dimensional cantilever beam under uniform loads. The next example will be an extension to a three dimensional case using a cantilever beam in tension.

Section 4.3 will be a further extension of elasticity using fracture mechanics, where the POD-RBF technique will be used to estimate the crack length of a compact tension specimen under ASTM E399 standards.

<u>4.1 - Heat Conduction</u>

The first set of applications to be covered will deal with the basic idea of conductive heat transfer. In order to set the premise for the rest of the examples, a simple heat conduction problem using a square block will be given in order to inversely estimate a spatially dependent thermal conductivity. This problem and its solutions will be outlined in detail with the later examples presented for broadness.

4.1.1 - Square Domain

In the first example, the POD-RBF network will be utilized to approximate the temperature distribution at points within a square block, shown in Figure 7, as well as estimate the spatially dependent thermal conductivity.
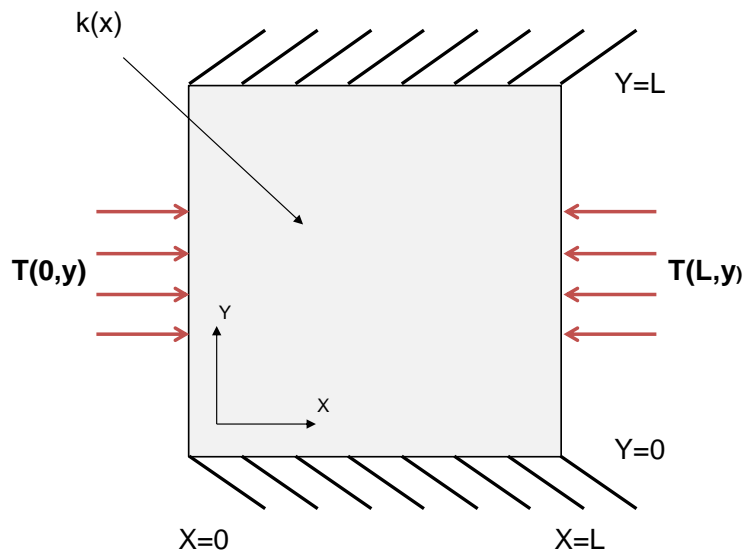

Figure 7 - Illustration of square domain for heat conduction case

The thermal conductivity in this first case is a linear function of the x (horizontal) direction and can be written as

$$k(x) = a + bx \tag{35}$$

where $k(x)$ denotes the thermal conductivity at some point x. This relation is used to establish the initial parameter matrix which will be referred to during RBF extrapolation. For our first application, the Hardy inverse RBF interpolation equation can be seen as

$$f_i\left(k(a,b)\right) = \frac{1}{\sqrt{k(a,b)^2 + c^2}} \tag{36}$$

where

$$k(a,b) = [a + bx] - p^i \tag{37}$$

which is used to approximate the temperature distributions $\mathbf{u}$ within the body.

$$u(a,b) \approx \phi \cdot B \cdot f\left(k(a,b)\right) \tag{38}$$

The temperature distributions (or the snapshot vector $\mathbf{u}$) are then used to estimate the constants of the spatially dependent thermal conductivity shown in (35), using the least squares objective function utilized by LM

$$J(p) = \left[\sum_{i=1}^{N}\left(u_i(p) - y_i\right)\frac{\partial u_i(p)}{\partial p}\right] + \alpha\left[\sum_{i=1}^{N}\left(u_i(p) - \bar{y}\right)\frac{\partial u_i(p)}{\partial p}\right] \tag{39}$$

where the vector $\mathbf{p}$ represents the thermal conductivity constants to be determined.

$$p = \begin{pmatrix} a \\ b \end{pmatrix} \tag{40}$$

For our initial validation case, the thermal conductivity constants are chosen to be $a = 1.234$ and $b = 3.456$. Although not described here, the direct heat conduction problem is solved using the following exact solution

$$T(x, y) = \frac{C}{b}\ln(a+bx) + Dy + E \tag{41}$$

where the constants C, D and E are chosen arbitrarily (but in this case were chosen as $C=100$, $D=10$ and $E = 0$). The snapshot matrix $\mathbf{U}$ is then set up using 16 equally spaced nodes N throughout the square region. A total of 100 snapshots M were created using various values of a and b to establish the thermal conductivity field $k(x)$, or the initial parameter matrix.

Performing POD on the covariance matrix $\mathbf{C}$ defined in (8) produces the following eigenvalues shown in Table 1, truncated after the 5th term of a possible 100.

Table 1 - Table of truncated eigenvalues of square region heat conduction case

λ
9.605×10^6
1.715×10^4
1.348×10^3
23.903
0.026

It is important to note that at this point, the approximation of the temperature field and thermal conductivity parameters $\mathbf{p}$ may not be accurately estimated. In order to achieve an accurate approximation, the selection of the regularization parameter α must be chosen. Initially this can

be accomplished by randomly selecting regularization constants and comparing the POD-RBF approximations to the analytical solution of the temperature field, as seen in Figure 8.

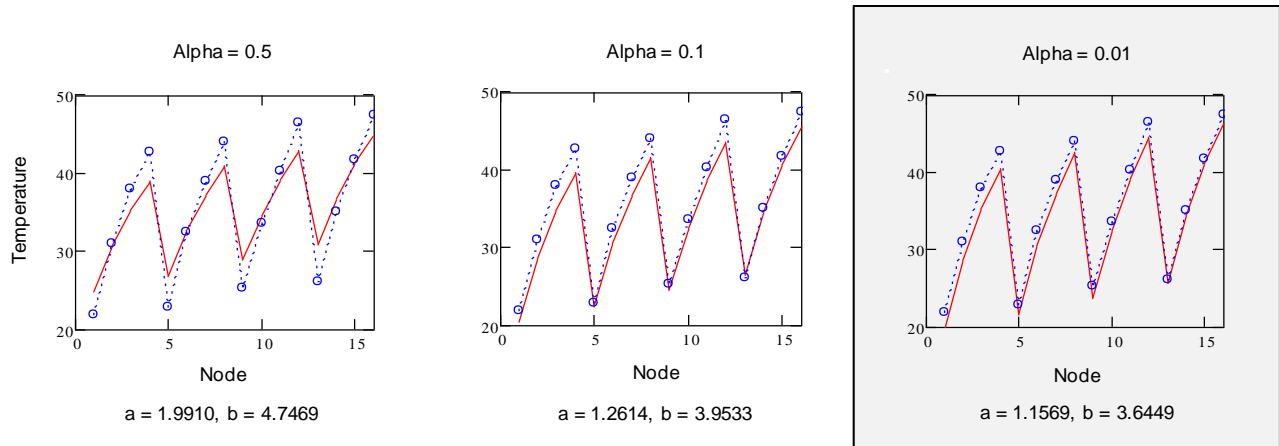Figure 8 - POD estimates of temperature distributions at various regularization constants for square region heat conduction

However, a more general case can be followed as it applies in [14]. This states that a regression optimization curve, shown in Figure 9, can be established utilizing the norm of the first and second term in (39).
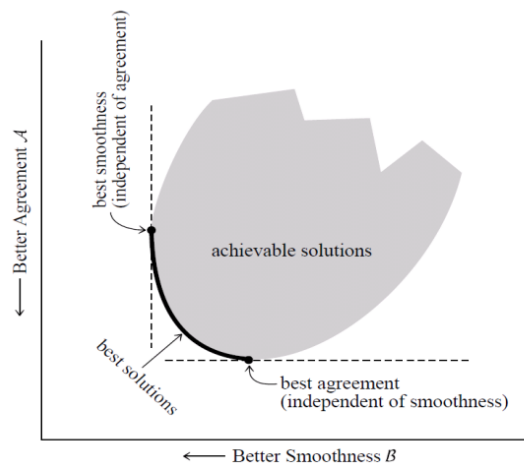
Figure 9 - Alpha optimization curve, courtesy of Numerical Recipes [14]

Applying this to our heat conduction problem yields Figure 10 below. The black box in Figure 10 denotes the optimal regularization value which is also highlighted in Figure 8 above. In this case the regularization parameter is chosen as $\alpha = 0.01$.
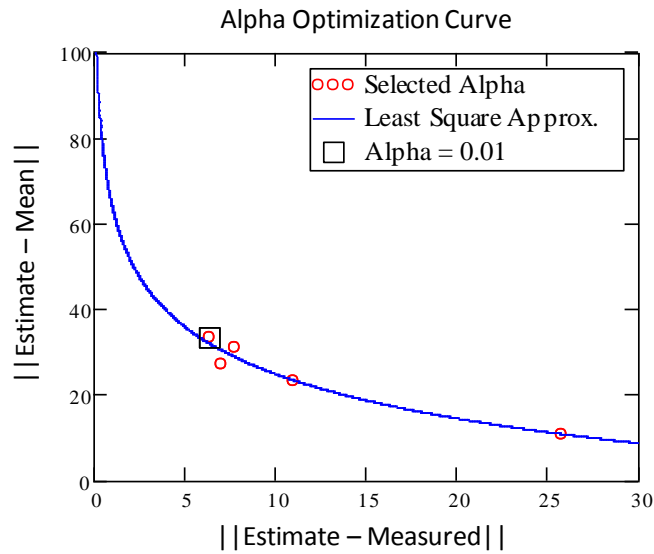
Figure 10 - Alpha optimization curve for simple heat conduction cases

After the regularization parameter is selected, the POD-RBF inverse approach can be fully implemented to accurately estimate the temperature distribution and thermal conductivity constants within the system. The POD-RBF estimation of the temperature distribution can be seen in Figure 11, while the error of the approximation is shown in Figure 12.

Comparison of POD Estimate versus
Measured Temperature Distribution
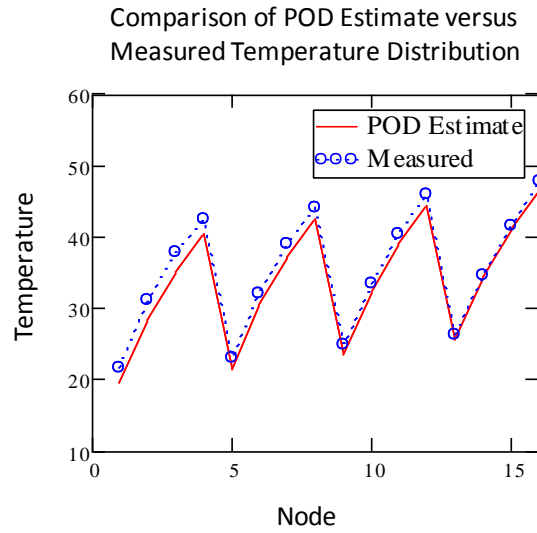
Figure 11 - Comparison of exact solution against POD estimation of temperature distribution for
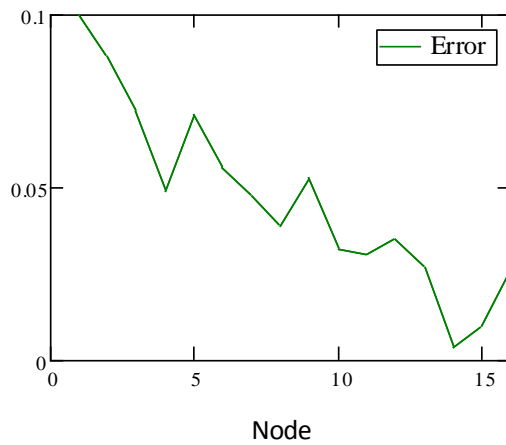
square region

Figure 12 - Error against POD-RBF solution to exact solution for square region

It can be seen that the error produced in the POD-RBF approximation is never larger the 10% for

this example. More importantly, the approximation of the thermal conductivity constants and its

distribution through the domain is shown below in Table 2 and Figure 13, respectively.

Table 2 - Comparison of Actual and POD-RBF estimation of thermal conductivity of square

region

	Actual	Estimate
a	1.234	1.169
b	3.456	3.668

Comparison of POD Estimate versus
Measured K(x)
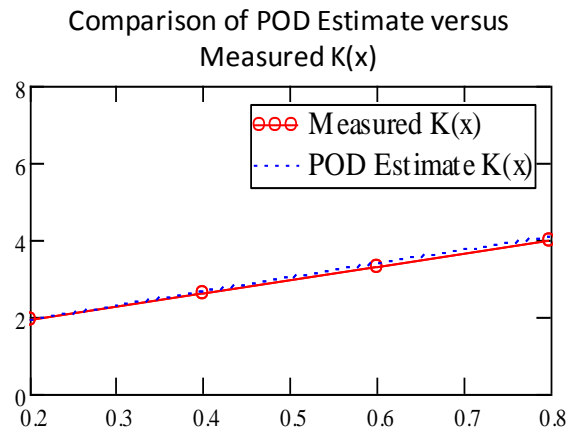
Figure 13 - Comparison of POD-RBF estimate of thermal conductivity against measured data for

square region

Accordingly, the POD-RBF inverse method produces an accurate approximation of the thermal

conductivity field as well as the temperature distributions within the square region. On the other

hand, this first case uses the exact analytical solution to generate the measured data field. In an

experimental sense, instrumentation error would create noise in the data reading which may skew

the POD-RBF approximation. In order to accommodate this, a random normal distribution error

is added to the analytical solution to represent instrumentation noise from data collection.

Noise is added to the exact temperature solution at $\pm 0.5^{o}$ and the POD-RBF inverse approach is then reapplied to the system. The corresponding results are shown in Figure 14 and Figure 15.

Comparison of POD Estimate versus
Measured Temperature Distribution

Figure 14 - Comparison of measured noisy ($\pm 0.5^{o}$) data against POD estimation of temperature

distribution for square region
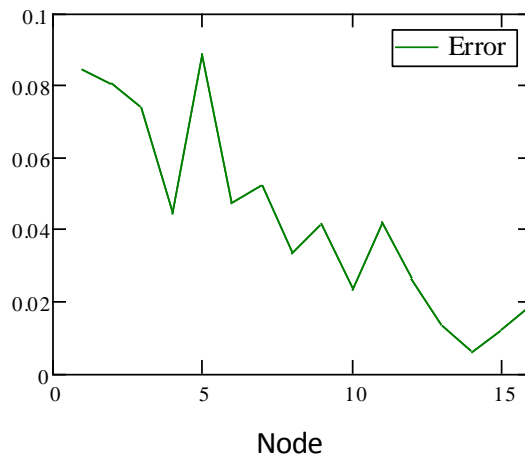
Figure 15 - Error against POD-RBF solution to measured noisy ($\pm 0.5^{o}$) data for square region

Once again, the temperature distribution is estimated accurately with only small amounts of error present in the approximation, as noted in the previous example. Moreover, the thermal conductivity is also estimated closely with minimal error as shown in Table 3 and Figure 16.

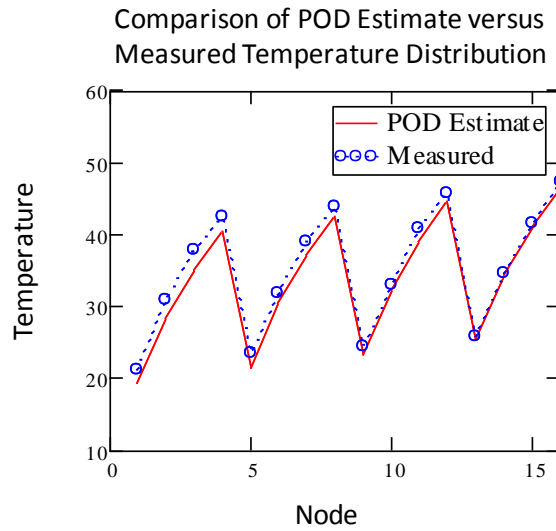Table 3 - Comparison of Measured and POD-RBF estimation of thermal conductivity of square region using noisy data ($\pm 0.5^o$)

	Actual	Estimate
a	1.234	1.157
b	3.456	3.645
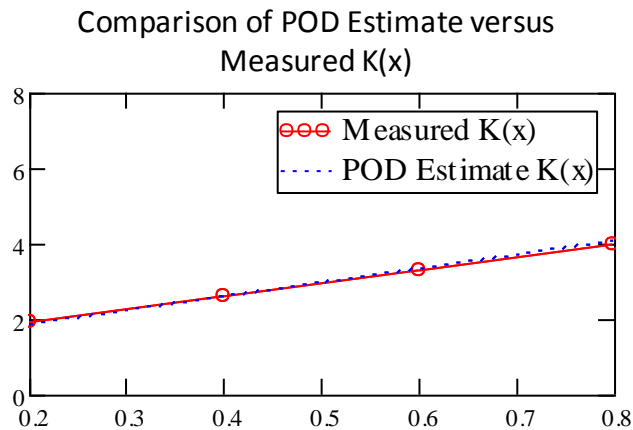
Figure 16 - Comparison of POD-RBF estimate of thermal conductivity against measured noisy ($\pm 0.5^o$) data for square region

Now referring back to Chapter 2.1, the POD basis vectors maintain some type of correlation to the original direct system. In the case of heat transfer, the POD basis vectors have some physical meaning and can be related to an analytical eigenfunction of the form

$$eig(x, y) = \sin\left(\frac{n\pi x}{L}\right)\cos\left(\frac{m\pi y}{L}\right) \qquad (42)$$

where x and y are physical locations throughout the domain and $n = 1, 2, 3...$ and $m = 0, 1, 2...$

Applying the analytical eigenfunction to the current square domain yields the following in Figure 17.
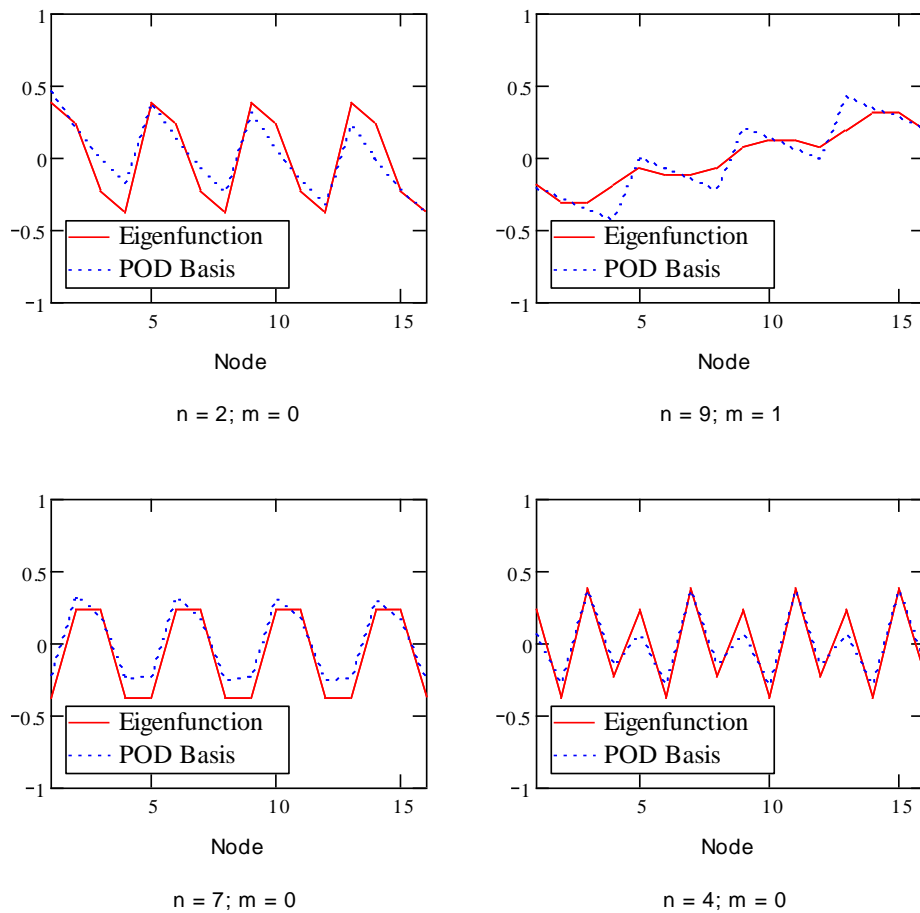
Figure 17 - Comparison of analytical eigenfunctions to POD basis vectors

Accordingly, this realization helps to show that the POD transformation does not lose all physical interpretation to the direct problem at hand. In a more complex sense, the POD basis

vectors may be used to represent the eigenfunctions, when an analytical solution is hard to derive effectively.

While these basic examples only outline the premise of the topic of the POD-RBF network it can be expanded into more complicated domains, as will be shown in future sections.

4.1.2 - L Shaped Domain

In this section, a variation of the previous heat conduction example will now be studied. For this case, the square region will be modified to represent an L shaped region as shown in Figure 18.

Figure 18 - Illustration of L shaped region for heat conduction case

Since the only change to the problem will be to the domain, the same POD-RBF derivations will be applied from Section 4.1.1. The main objective of this section is to study how the change in domain shape will affect the POD-RBF approximation, if any.

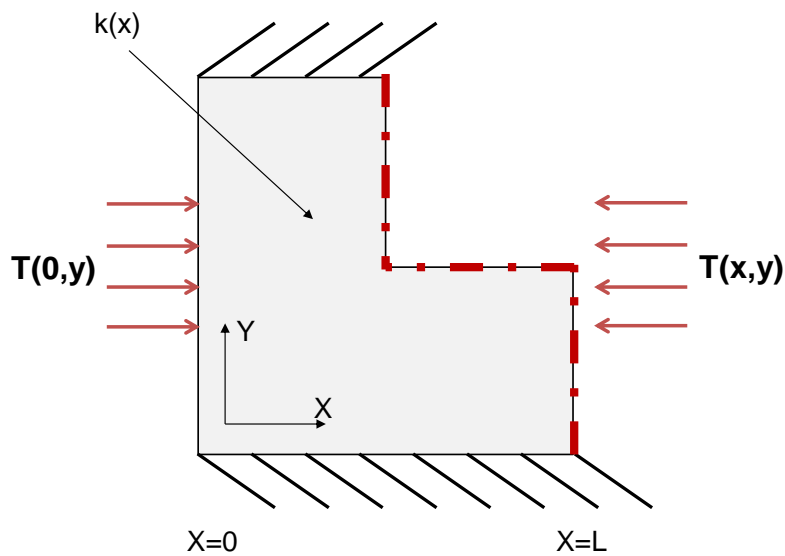The temperature field was set up using 12 nodes spaced throughout the domain using 100 snapshots to create the thermal conductivity field $k(x)$ and snapshot matrix $\mathbf{U}$. Performing POD on the covariance matrix $\mathbf{C}$ produced the following eigenvalues shown in Table 4, truncated after the 5th term (of 100).

Table 4 - Table of truncated eigenvalues of L region heat conduction case

λ
6.560×10^6
9.623×10^4
1.032×10^3
18.241
0.015

Unlike Section 4.1.1, an alpha optimization curve will not be generated for this example. Based on similarities to the previous problem, the same regularization parameter α will be used ($\alpha = 0.01$). Doing so now allows for the POD-RBF inverse technique to be applied in order to estimate the temperature field and thermal conductivity field, respectively.

The first case studied will have no noise added to the solution for initial verification. The results are shown below in Figure 19 - Figure 21.

Comparison of POD Estimate versus
Measured Temperature Distribution

Figure 19 - Comparison of measured data against POD estimation of temperature distribution for

L region

Error between POD Estimated and
Measured Temperature Distribution

Figure 20 - Error against POD-RBF estimate to measured data for L region
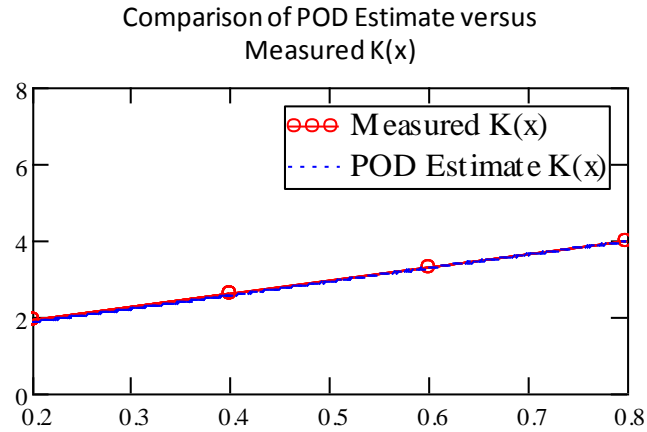
Figure 21 - Comparison of POD-RBF estimate of thermal conductivity against measured data for

L region

Again the temperature distribution and thermal conductivity are estimated precisely using the POD-RBF technique, despite the shape of the domain. A maximum error just above 10% is shown in Figure 20 which is still extremely accurate considering only 5 eigenvalues were used to estimate the system. Accordingly, the newly approximated constants for the L region are shown in Table 5 below.

Table 5 - Comparison of Measured and POD-RBF estimation of thermal conductivity of L region

	Actual	Estimate
a	1.234	1.182
b	3.456	3.486

For the next case studied, a small amount of noise (± 0.5°) will be incorporated into the solution to act as empirical data. The corresponding results are shown below in Figure 22 - Figure 24.
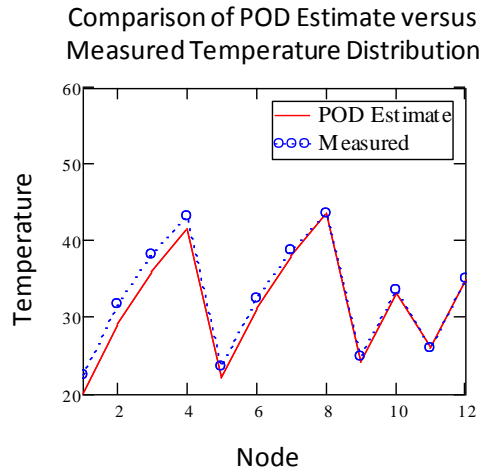

Figure 22 - Comparison of measured noisy (± 0.5°) data against POD estimation of temperature
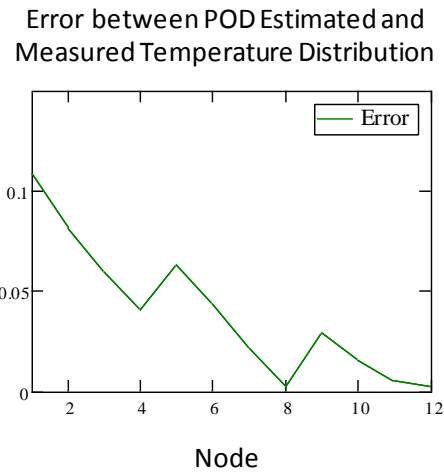
distribution for L region

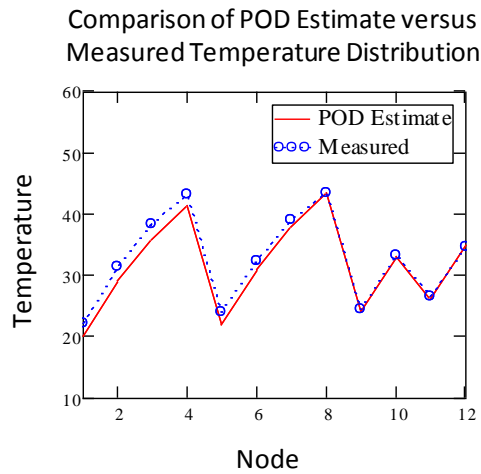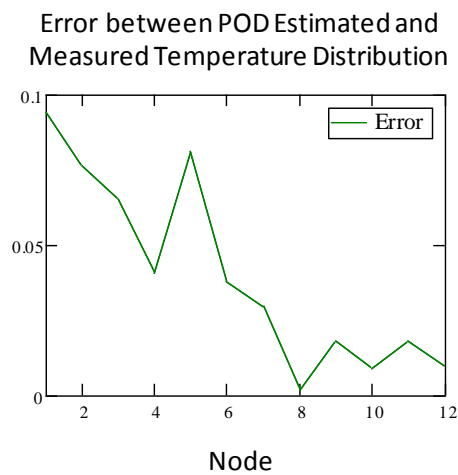
Figure 23 - Error against POD-RBF solution to measured noisy (± 0.5°) data for L region
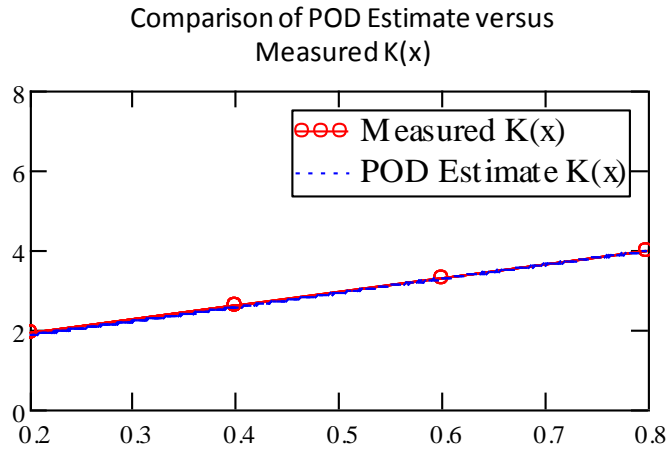
Figure 24 - Comparison of POD-RBF estimate of thermal conductivity against measured noisy ($\pm 0.5^{o}$) data for L region

Despite the small amount of noise present in the data, the POD-RBF network was still able to estimate the temperature field and thermal conductivity quickly and effortlessly. The estimated thermal conductivity constants, with a small amount of noise ($\pm 0.5^{o}$) added into the solution, are shown in Table 6.

Table 6 - Comparison of Measured and POD-RBF estimation of thermal conductivity of L region

	Actual	Estimate
a	1.234	1.177
b	3.456	3.504

In comparison to Section 4.1.1, the POD-RBF method still produces accurate results despite the shape of the domain being used. This is great news as it will allow the POD-RBF method to take on much more complicated domains.

As done in the section 4.1.1, the POD basis vectors can be shown to have a direct correlation to the eigenfunctions represented in (42). Using the same ideology outlined previously, the analytical eigenfunctions in an L shaped domain are represented in Figure 25.
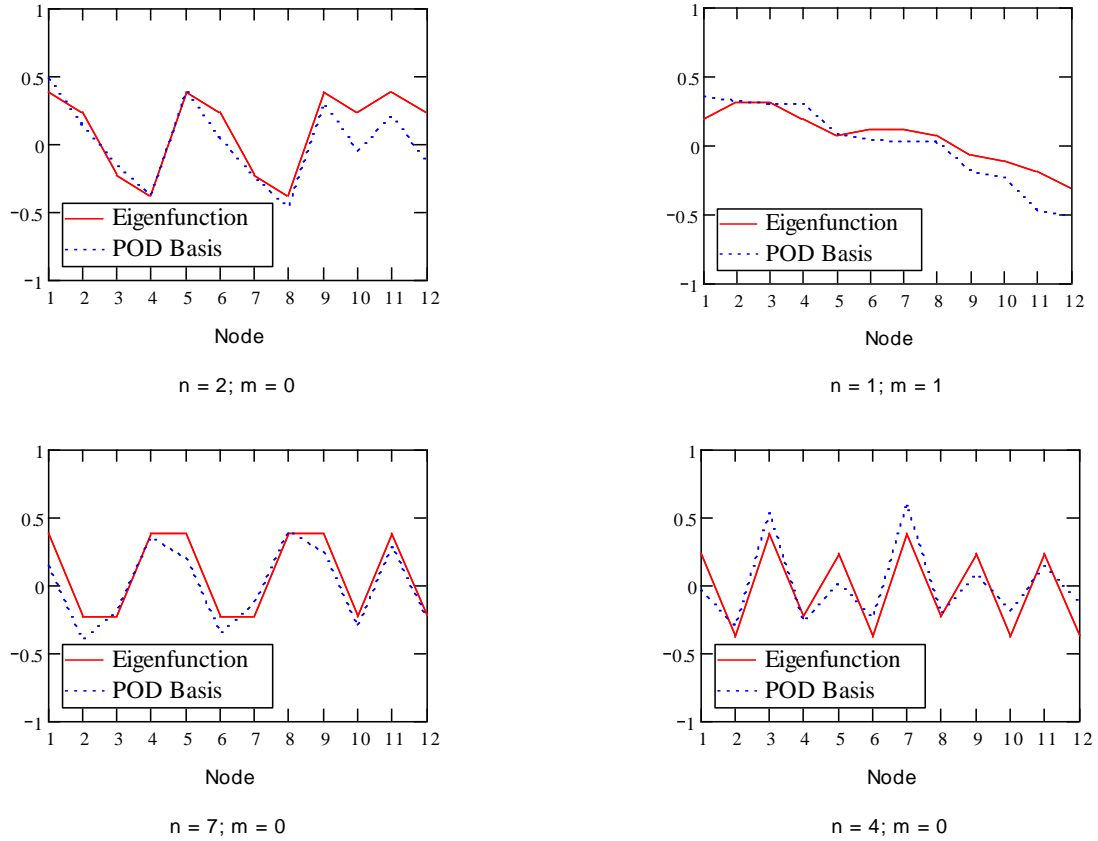
Figure 25 - Comparison of analytical eigenfunctions to POD basis vectors in L shaped domain

4.1.3 - Complex Domain

For the complex domain example, we will now consider a spatially varying thermal conductivity that is dependent on both the *x* and *y* Cartesian directions. Moreover, the analytical

solution to a problem of this nature is not readily available by simple derivation. As a result, BEM will be implemented in order to generate the snapshot data **u**. An illustration of the complex domain is shown in Figure 26.
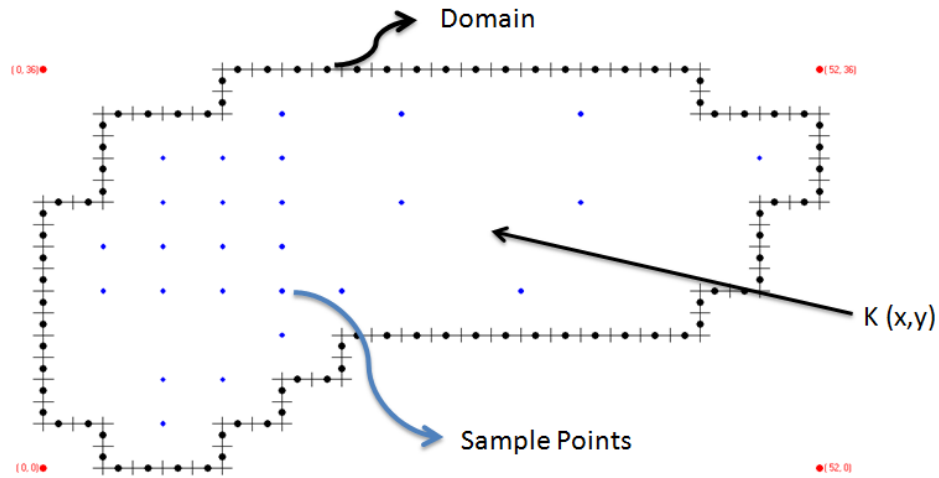
Figure 26 - Illustration of complex domain in heat conduction

As stated above, the thermal conductivity in this case is a spatially dependent in the *x* and *y* direction and is written as

$$k(x, y) = a_1 + a_2 x + a_3 y^2 \tag{43}$$

where *k(x,y)* denotes the thermal conductivity at points *x* and *y*. Analogous to the previous examples, (43) is used to establish the initial parameter matrix for RBF extrapolation; whereby the RBF interpolation function can be rewritten as

$$f_i\left(k\left(a_1, a_2, a_3\right)\right) = \frac{1}{\sqrt{k\left(a_1, a_2, a_3\right)^2 + c^2}} \tag{44}$$

with

$$k(a_1, a_2, a_3) = \left[a_1 + a_2 x + a_3 y^2 \right] - p^i \tag{45}$$

In which the temperature distributions **u** are approximated within the complex domain using

$$u(a_1, a_2, a_3) \approx \phi \cdot B \cdot f\left(k(a_1, a_2, a_3) \right) \tag{46}$$

Similarly, temperature distributions are used to estimate the parameters **p**, using the least squares objective function inside LM.

$$J(p) = \left[\sum_{i=1}^{N} \left(u_i(p) - y_i \right) \frac{\partial u_i(p)}{\partial p} \right] + \alpha \left[\sum_{i=1}^{N} \left(u_i(p) - \bar{y} \right) \frac{\partial u_i(p)}{\partial p} \right] \tag{47}$$

The parameter vector **p** represents now represents the three thermal conductivity constants to be determined.

$$p = \begin{pmatrix} a_1 \\ a_2 \\ a_3 \end{pmatrix} \tag{48}$$

However, in this case it is not entirely necessary to estimate the parameters **p** exactly. It is our goal to accurately estimate the thermal conductivity field at the sampled points within the domain shown in Figure 26.

The snapshot matrix **U** was assembled using 26 randomly spaced nodes throughout the domain and 125 snapshots were taken at various thermal conductivity values. Now performing POD on the covariance matrix generates the following eigenvalues truncated after the 4th term (of a possible 125) as shown in Table 7.

Table 7 - Table of truncated eigenvalues of complex domain heat conduction case

λ
1.21×10^6
157.82
0.581
0.106

Of course before the POD-RBF method is used for approximations, an alpha optimization curve is generated in order to achieve the best solutions denoted in Figure 9. For this case, the alpha optimization curve is shown in Figure 27.
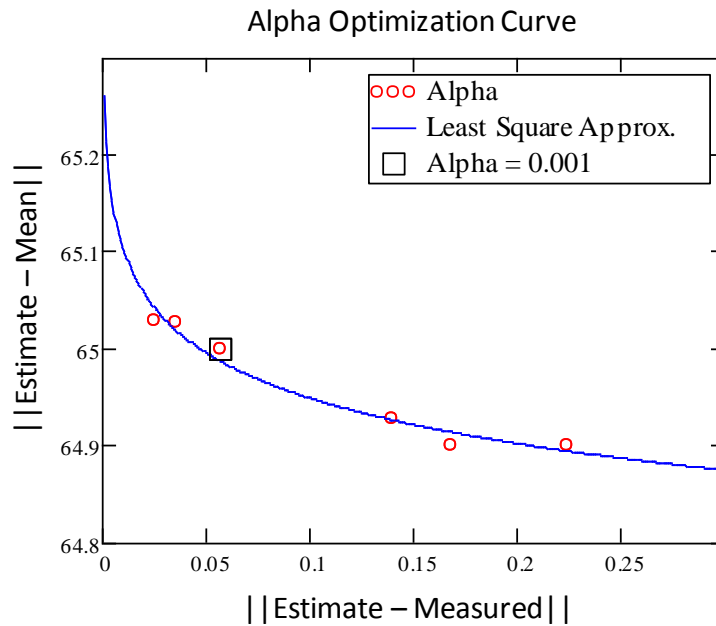
Figure 27 - Alpha optimization curve for complex domain case for heat conduction

As denoted in the above figure, the optimal regularization value is chosen at $\alpha = 0.001$. Afterwards, noise is then added to the BEM solution at $\pm 0.5^o$ to represent instrumentation error.

Applying the POD-RBF network yielded the following temperature distributions and errors shown in Figure 28 and Figure 29 respectively. The thermal conductivity is also estimated accurately across the domain as shown in Figure 30 with the corresponding error plot shown in Figure 31.

Figure 28 - Comparison of measured noisy ($\pm 0.5^o$) data against POD estimation of temperature distribution for complex domain

Figure 29 - Error against POD-RBF solution to measured noisy ($\pm 0.5^o$) data for complex domain

Figure 30 - Comparison of measured thermal conductivity against POD-RBF estimation using

noisy (± 0.5°) temperature distribution data for complex domain

Figure 31 - Error against POD-RBF estimate of thermal conductivity to measured thermal

conductivity using noisy (± 0.5°) data for complex domain

As illustrated in Figure 28 - Figure 31, the POD-RBF technique provides an excellent

approximation of the temperature and thermal conductivity field despite the existence of error.

45

Although this statement was verified in previous heat conduction examples, it still remains valid in the accompaniment of a complex domain and a more indirect problem.

For further robustness, noise of $\pm 2.0^o$ is now added to the BEM solution to see how the POD-RBF network reacts in the presence of large amounts of noise within the data. The following results are shown in Figure 32 - Figure 35.
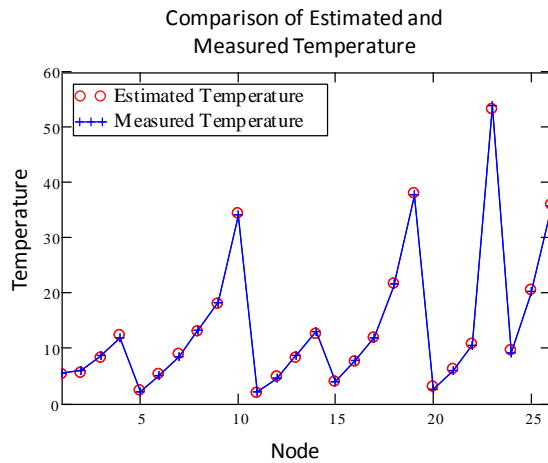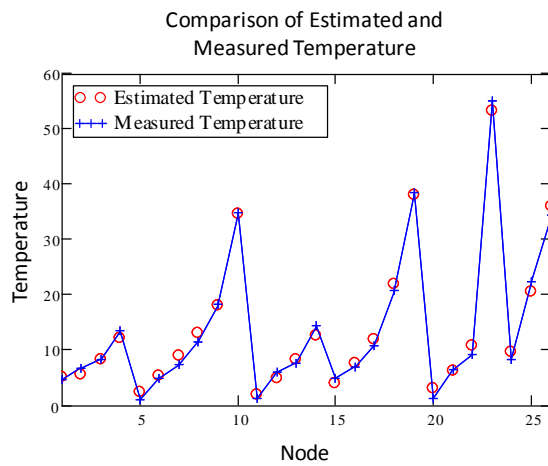

Figure 32 - Comparison of measured noisy ($\pm 2.0^o$) data against POD estimation of temperature
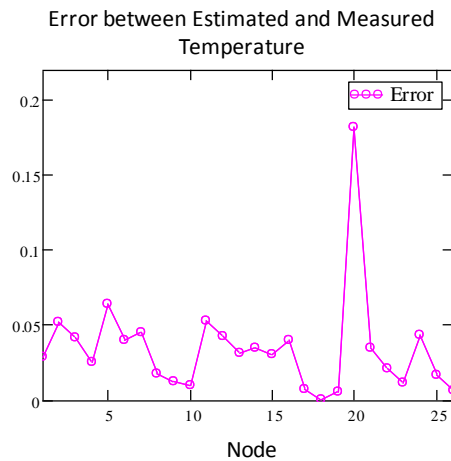
distribution for complex domain
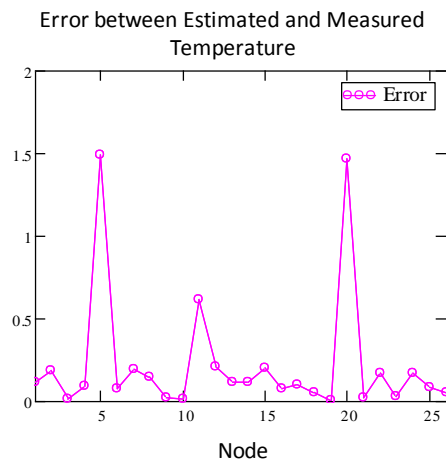
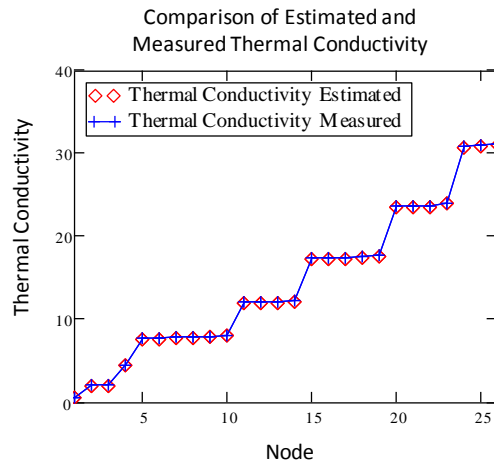Figure 33 - Error against POD-RBF solution to measured noisy ($\pm 2.0^o$) data for complex domain
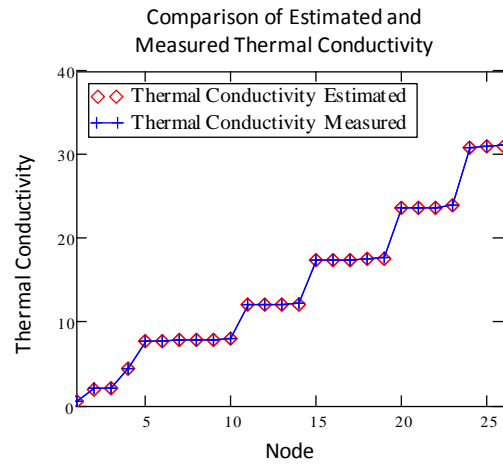
Figure 34 - Comparison of measured thermal conductivity against POD-RBF estimation using noisy ($\pm 2.0^{o}$) temperature distribution data for complex domain
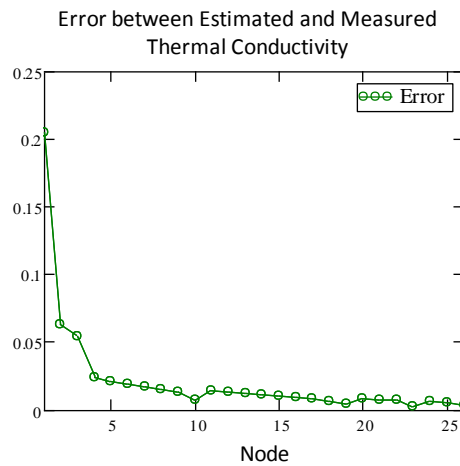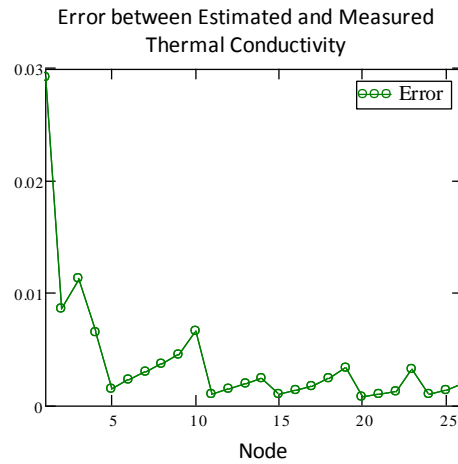

Figure 35 - Error against POD-RBF estimate of thermal conductivity to measured thermal conductivity using noisy ($\pm 2.0^{o}$) data for complex domain

Although there are spikes in the error present due to the additional noise added, the POD-RBF inverse approach still provides an excellent estimation of the temperature field and thermal

conductivity through the sampled points. In fact, this further helps to show that the POD-RBF technique is quite insensitive to noise inside the data, as also reported by [11][16].

<u>4.2 - Elasticity</u>

The next series of applications will use the POD-RBF inverse technique to accurately estimate the modulus of elasticity, shear modulus and Poisson's ratio of a two dimensional and three dimensional bar set up. Using basic relations from linear elasticity, the three material parameters are related using

$$E = 2G(1+v)$$ (49)

where E, G and v denote the modulus of elasticity, the shear modulus and Poisson's ratio respectively. This governing relation will be used to establish the initial parameter matrix which will be referred to during RBF extrapolation for the inverse approximation. For the elasticity applications, the RBF interpolation equation can be seen as

$$f_i(r(G,v)) = \frac{1}{\sqrt{r(G,v)^2 + c^2}}$$ (50)

where

$$r(G,v) = \left[2G(1+v)\right] - p^i$$ (51)

which is used to approximate the deformations **u** within the body.

$$u(G,v) \approx \phi \cdot B \cdot f(r(G,v))$$ (52)

The deformation approximation is now used to inversely estimate the material parameters using the least squares objective function implemented in LM

$$J(p) = \left[\sum_{i=1}^{N}\left(u_i(p) - y_i\right)\frac{\partial u_i(p)}{\partial p}\right] + \alpha\left[\sum_{i=1}^{N}\left(u_i(p) - \bar{y}\right)\frac{\partial u_i(p)}{\partial p}\right] \tag{53}$$

where **p** is a vector of the material properties

$$p = \begin{pmatrix} G \\ \nu \end{pmatrix} \tag{54}$$

It should further be noted, that using the elastic relation in (49) only two material parameters need to be used since the third property can be determined using the isotropic relation.

4.2.1 - Two Dimensional Cantilevered Beam

The first elasticity application utilizes a two dimensional cantilever beam under a uniform load P shown in Figure 36 to solve for the unknown elastic properties. In the case a validation, the selection of the material had the following elastic properties $E = 156\ GPa$, $G = 60\ GPa$ and $\nu = 0.30$.
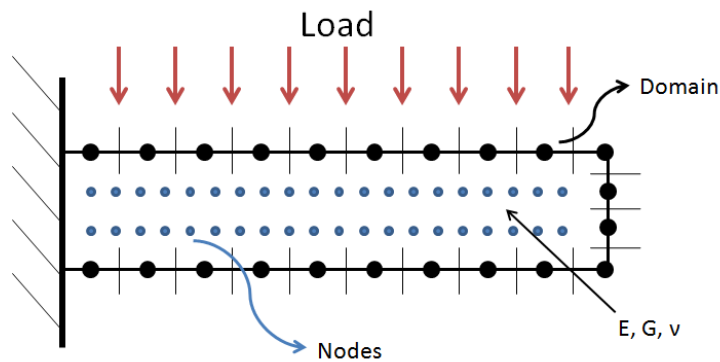
Figure 36 - 2D BEM Model of Cantilevered Beam

The direct problem was solved using BEM to generate the deflections in the y (vertical) direction on the discretized mesh. The snapshot matrix **U** was assembled using 520 equally spaced nodes throughout the beam with 100 snapshots at various parameters **p**. POD was then performed on the covariance matrix **C** to yield the following eigenvalues in Table 8 truncated after the 5th term of a possible 100.

Table 8 - Table of truncated eigenvalues for 2D elasticity case

λ
1.275×10^{9}
244.737
0.113
5.813×10^{-5}
5.536×10^{-5}

Now similar to the heat transfer cases, the regularization constant α needs to be determined in order to produce an accurate least squares fit of the data. Figure 37 (a) - (c) shows the selection of α at various regularization values, as well as how well they approximated the actual modulus of elasticity (E = 156 GPa).

α = 0.01

E = 175.4 GPa

(a)

α = 0.005

E = 158.8 GPa

(b)

α = 0.001

E = 166.3 GPa
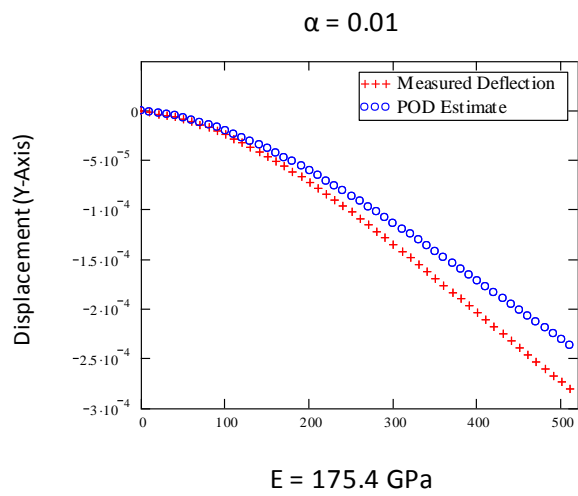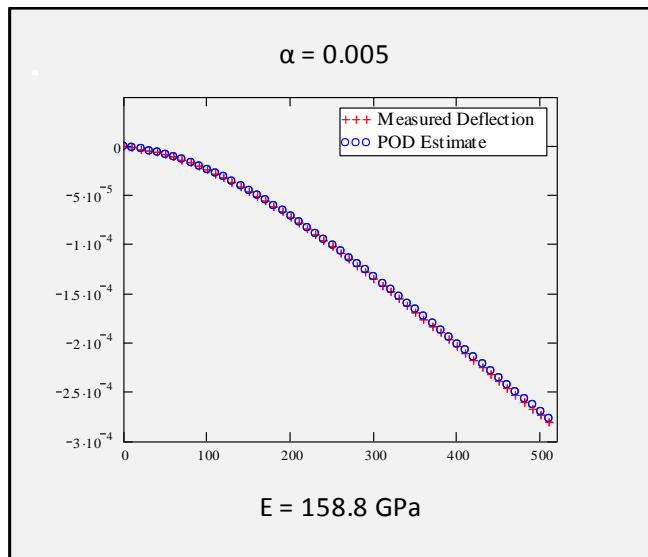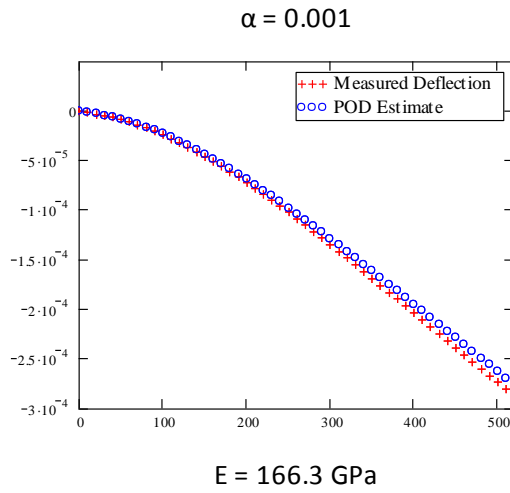
(c)

Figure 37 - POD estimation of the deflections at various regularization constants for 2D elasticity; (a) *α = 0.01*, (b) *α = 0.005*, (c) *α = 0.001*

In a more general case, the alpha optimization curve can be generated as done in the heat conduction examples. For elasticity, the alpha optimization curve is shown in Figure 38.
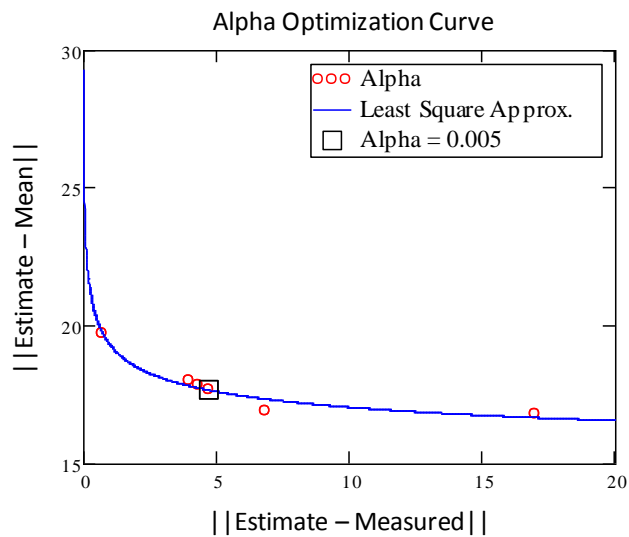
Figure 38 - Alpha optimization curve for 2D elasticity case

Utilizing Figure 37 and Figure 38 now allows for an ideal selection of the regularization parameter for the least squares approximation during the inverse procedure. It can be seen that the optimal regularization parameter is chosen as $\alpha = 0.005$ as it leads to a good fit of the numerical (or experimental) data. Comparing the POD-RBF approximation of the deflection against the actual BEM deflection is shown in Figure 39.
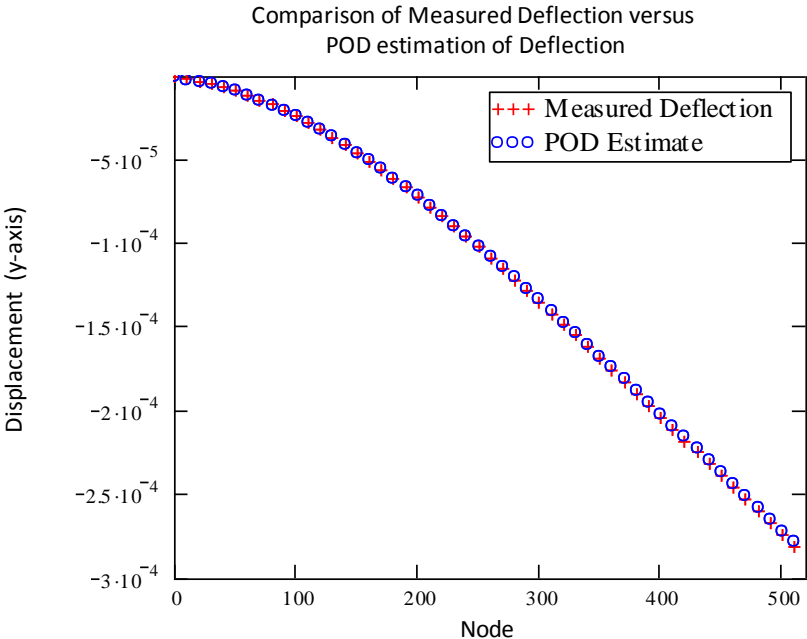
Figure 39 - Comparison of BEM deflection against POD-RBF estimation of deflection for 2D elasticity

The POD-RBF solution also produced the following elastic parameters shown in Table 9, which are compared to the actual material parameters used in the BEM solution.

Table 9 - Comparison of Actual and POD-RBF estimation of material parameters for 2D

elasticity

	Actual	Estimate
Modulus of Elasticity, E	156 GPa	152.8 GPa
Shear Modulus, G	60 GPa	61 GPa
Poisson's ratio, v	0.30	0.25

Moreover, the total error recorded from the POD-RBF approximation against the BEM solution

is shown in Figure 40.
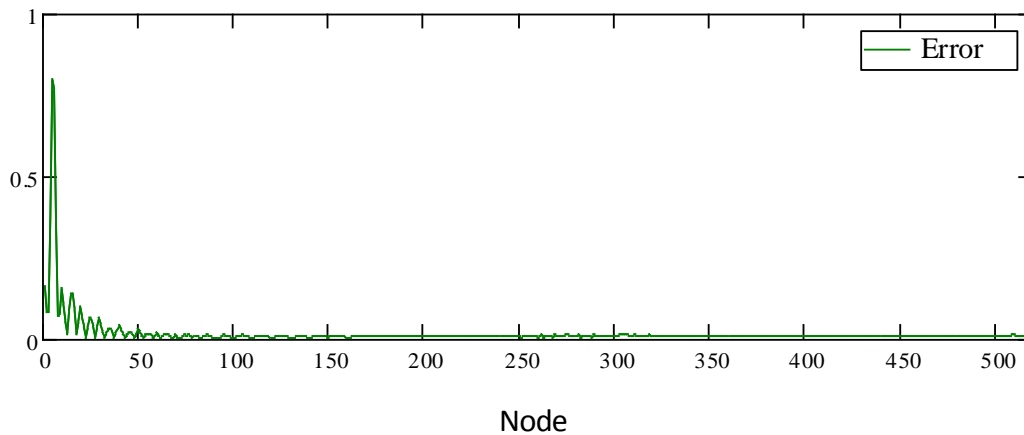
Figure 40 - Error against POD-RBF solution to BEM solution for 2D elasticity

It can be seen that there is a large initial error at the first few nodes but the error drops off

significantly at later nodes. This may be attributed to the cantilevered effect as a boundary

condition on the left side with the first few nodes.

Of course the above experiment was completed for an "ideal" numerical simulation. In an

experimental sense, there will be noise created from data collection. For further validation, the

POD-RBF inverse process will now be applied to the same problem with the addition of random noise ranging from ± 10 - 100 μm.

First error was added using a random normal distribution at ± 10 μm. Applying the POD-RBF inverse method yielded the following results shown in Figure 41 and Figure 42.

Figure 41 - Comparison of POD-RBF estimate of deflection against noisy data measurements (±10 μm) for 2D elasticity
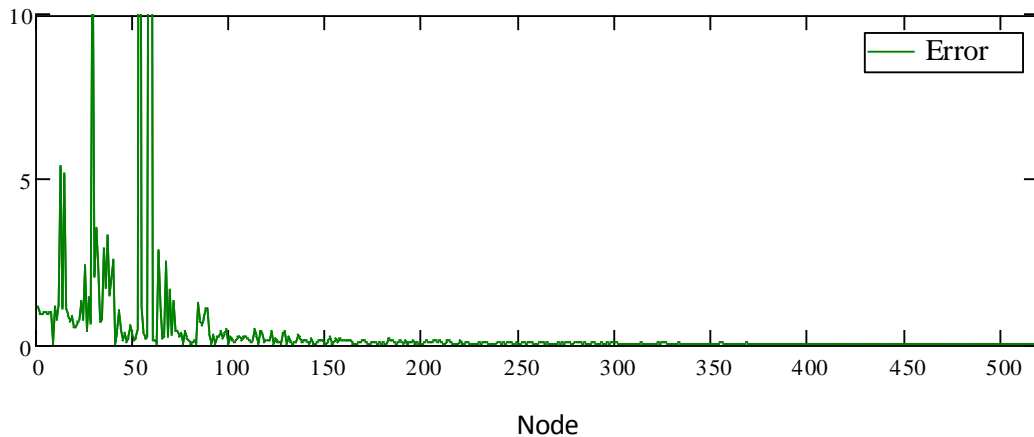
Figure 42 - Error against POD-RBF solution to noisy data (± 10 μm) measurements for 2D elasticity

Despite the presence of small amounts of noise in the data, the POD-RBF approximation was still able to achieve a good estimate of the material parameters. The material property estimates with small amounts of noise in the data ($\pm$ 10 μm) are shown in Table 10.

Table 10 - Comparison of Actual and POD-RBF estimation of material parameters with the addition of noisy data ($\pm$ 10 μm) measurements for 2D elasticity

	Actual	Estimate
Modulus of Elasticity, E	156 GPa	158.82 GPa
Shear Modulus, G	60 GPa	63.4 GPa
Poisson's ratio, ν	0.30	0.25

It can still be seen that despite the addition of small amounts of random noise to the BEM solution, the POD-RBF inverse technique was still able accurately estimate the material parameters of the system.

Now the amount of noise added into the solution is changed to $\pm$ 25 μm. Reapplying the POD-RBF inverse technique produced the following results in Figure 43 and Figure 44.
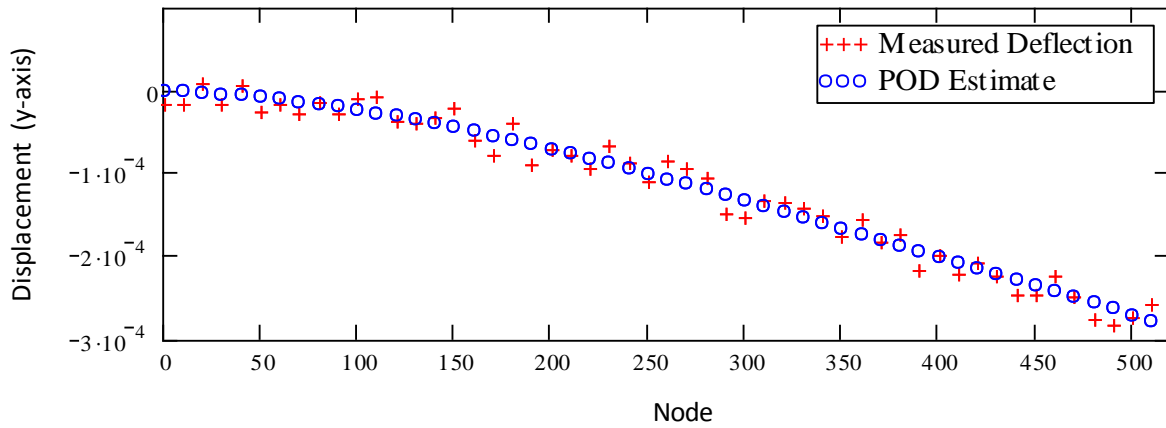
Figure 43 - Comparison of POD-RBF estimate of deflection against noisy data measurements (±
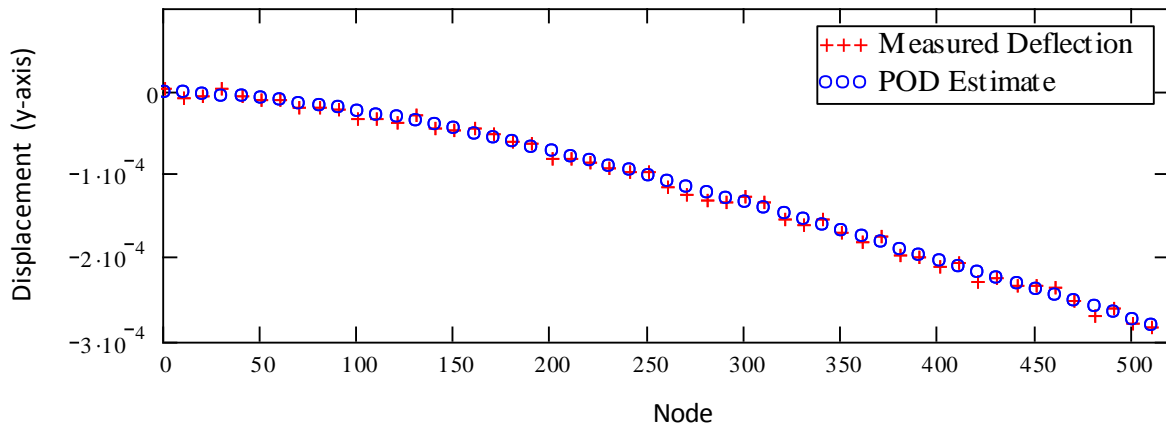
25 μm) for 2D elasticity
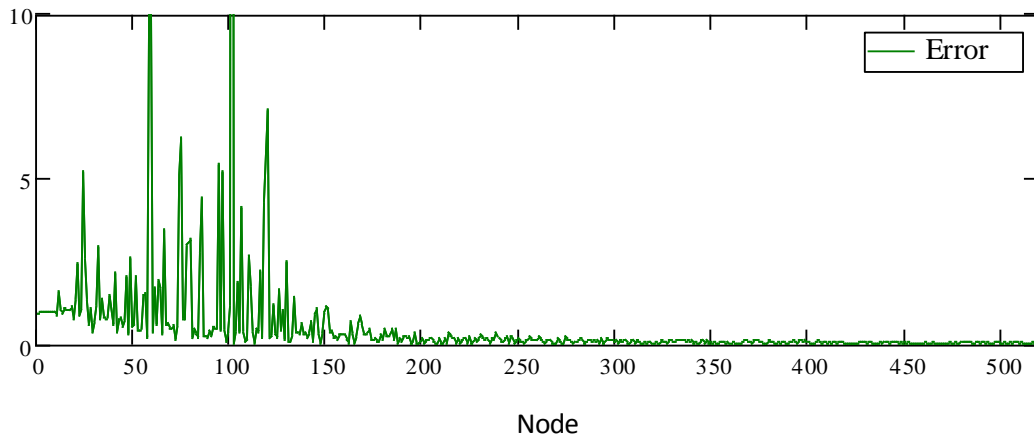
Figure 44 - Error against POD-RBF solution to noisy data (± 25 μm) measurements for 2D

elasticity

It may be noted, that the larger errors present in Figure 44 mainly appear due to the addition of

larger noise in the solution. Furthermore, this additional noise had little effect on the POD-RBF

approximation of the material parameters shown in Table 11.

Table 11 - Comparison of Actual and POD-RBF estimation of material parameters with the

addition of noisy data (± 25 μm) measurements for 2D elasticity

	Actual	Estimate
Modulus of Elasticity, E	156 GPa	160.01 GPa
Shear Modulus, G	60 GPa	63.6 GPa
Poisson's ratio, v	0.30	0.26

For further verification of the robust nature of the POD-RBF inverse approach in the field of elasticity; a large impractical amount of random noise (± 100 μm) will be added to the BEM solution. The POD-RBF approximation of the deflections is shown in Figure 45.
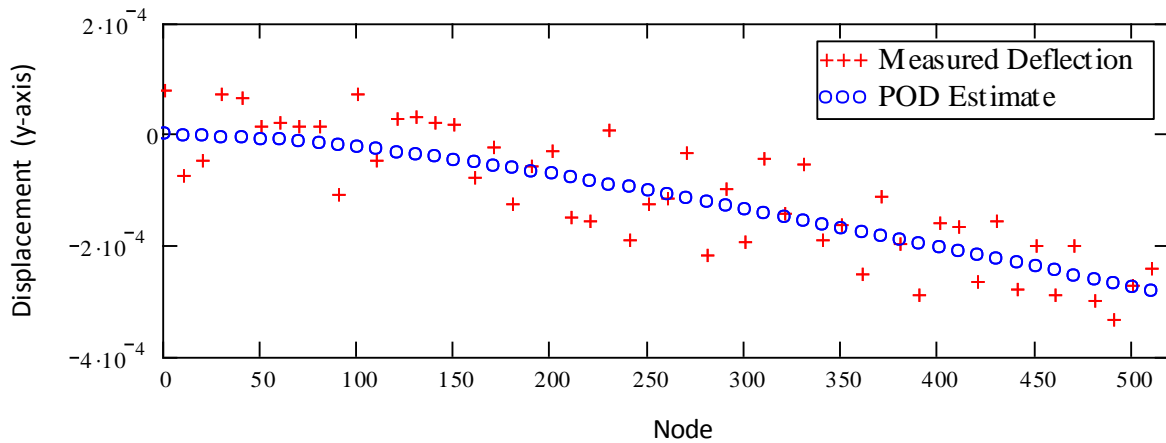
Figure 45 - Comparison of POD-RBF estimate of deflection against noisy data measurements (± 100 μm) for 2D elasticity

Observing Figure 45 also illustrates how the least squares fit goes through the mean value of the experimental (or noisy) solution as denoted from the original objective function shown in (53). A set of contour plots can be seen in Figure 46 to demonstrate how the POD-RBF approach creates

a smooth approximation (Figure 46 *bottom*) of the data even in the presence of large noise (Figure 46 *top*).
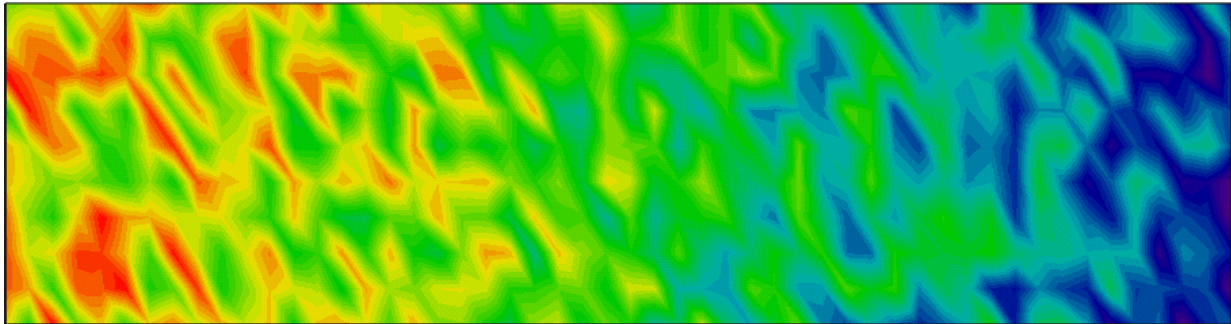
Measured
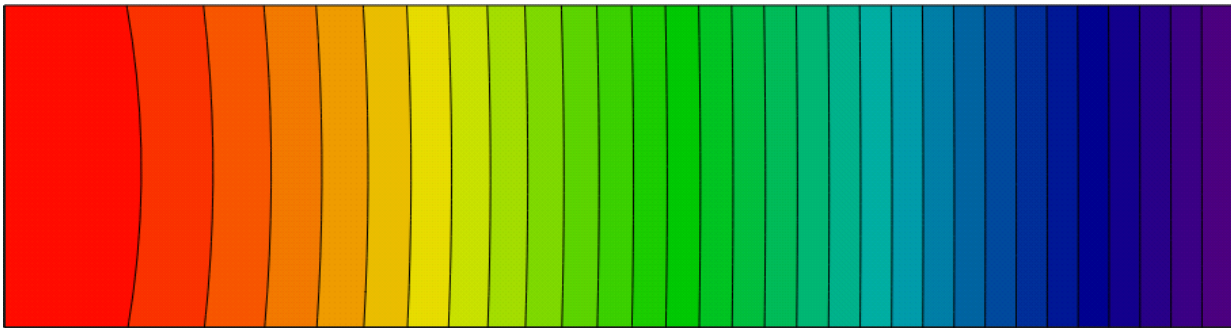
Estimate

Figure 46 - Contour plot of 2D cantilevered beam with noisy solution (top) and POD-RBF approximation (bottom)

The approximation of the material properties are shown in Table 12 and still produce remarkably accurate estimates of the elastic constants.

Table 12 - Comparison of Actual and POD-RBF estimation of material parameters with the

addition of noisy data (± 100 μm) measurements for 2D elasticity

	Actual	Estimate
Modulus of Elasticity, E	156 GPa	152.45 GPa
Shear Modulus, G	60 GPa	60.3 GPa
Poisson's ratio, v	0.30	0.26

4.2.2 - Three Dimensional Bar

Now let us consider an extension of the two dimensional elasticity problem to a three dimensional example shown in Figure 47. The deflections are set up to be extracted at the elemental points on the beam in order to replicate the placement of strain gages on the body. The actual elastic constants for this material are given as *E = 206.85 GPa, G = 80.8 GPa* and *v = 0.28.*
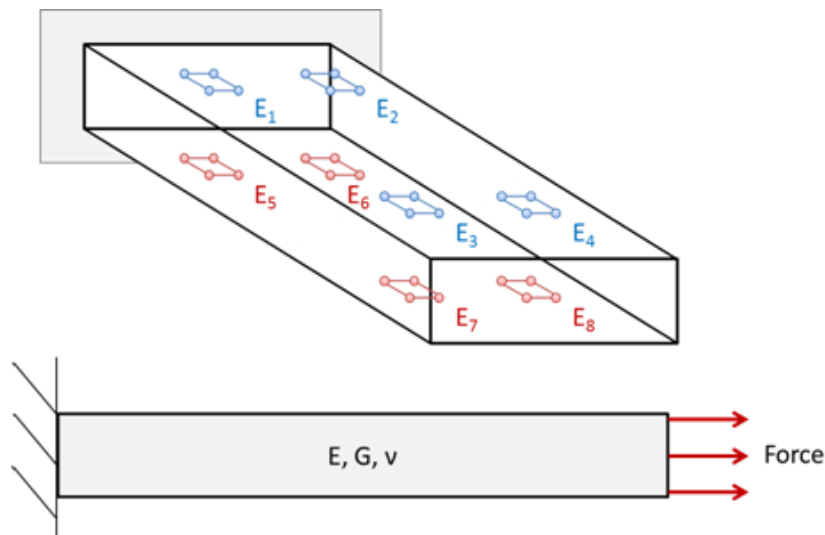
Figure 47 - 3D bar in tension

This time the direct problem was solved using FEM to generate the deflections in all Cartesian directions at the elemental locations shown in Figure 47. The snapshot matrix $\mathbf{U}$ was created using 128 nodes on the surface of the beam, taking a total 81 snapshots at varying elastic parameters $\mathbf{p}$. POD was then performed to produce the eigenvalues shown in Table 13 which were truncated after the 6th term of a possible 81.

Table 13 - Table of truncated eigenvalues for 3D elasticity case

λ
5.12×10^6
87.265
0.478
0.425
0.293
0.256

In order to avoid redundancy, the same regularization parameter shown in Figure 38 will be used for the three dimensional case inside of the least square objective function (53). Using this assumption the POD-RBF approximation can be compared to the direct FEM solution as shown in Figure 48 and Figure 49. Accordingly, Figure 48 includes the deflections in each Cartesian direction on the same plot; whereas Figure 49 shows each deflection direction individually.
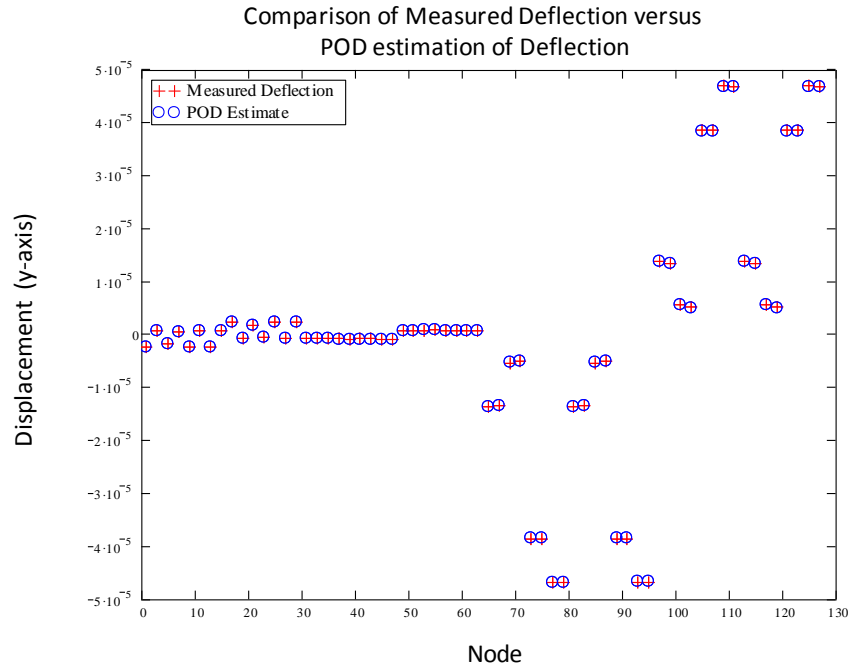
Figure 48 - Comparison of FEM solution against the POD-RBF approximation of the deflection

in 3D elasticity
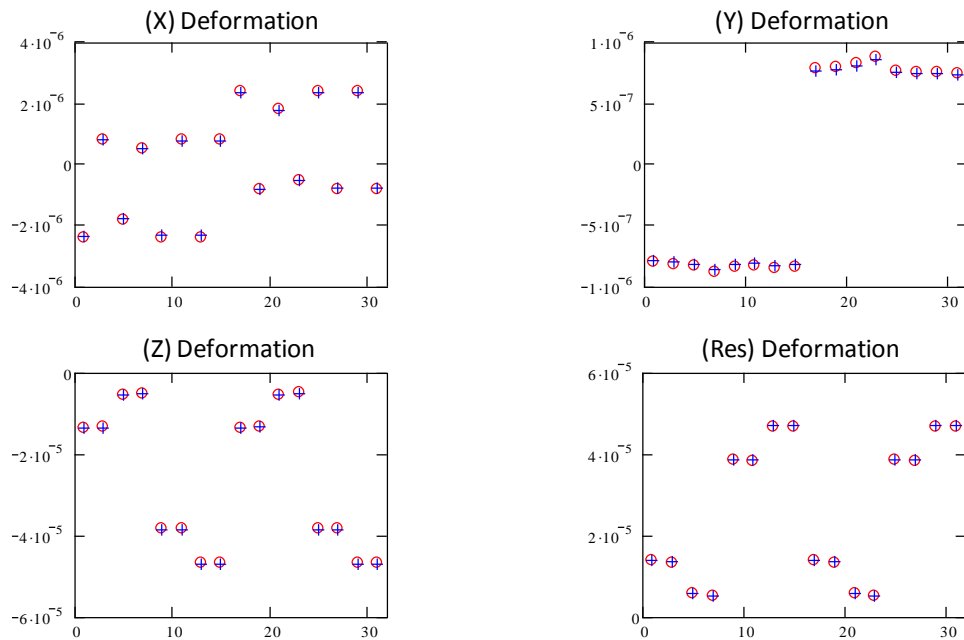
Figure 49 - Comparison of FEM solution against POD-RBF approximation in each Cartesian

direction for 3D elasticity

Likewise, the POD-RBF approach was able to accurately capture the material constants of the

three dimensional application as shown in Table 14.

Table 14 - Comparison of Actual and POD-RBF estimation of material parameters for 3D

elasticity

	Actual	Estimate
Modulus of Elasticity, E	206.85 GPa	200.75 GPa
Shear Modulus, G	80.8 GPa	77 GPa
Poisson's ratio, ν	0.28	0.3

Of course this first example provides only a verification of the technique as it uses no noise with respect to the FEM solution. In order to reproduce experimental data collection, noise will be added to the FEM solution as done in the previous sections.

The first amount of noise introduced used a random normal distribution of ± 1 μm. Applying the POD-RBF inverse technique produced the following results in Figure 50.

Figure 50 - Comparison of the POD-RBF approximation against the noisy data (± 1 μm) in each Cartesian direction for 3D elasticity

It can easily be seen that the introduction of small amounts of noise into this example produces a large observable change in the deformations in some directions. This is due to the small nature of the deflections; however, this magnitude of error is common in many industrial strain gages. Nevertheless, the POD-RBF technique still manages to accurately estimate the material constants of the bar as shown in Table 15.

Table 15 - Comparison of Actual and POD-RBF estimation of material parameters for noisy data

(± 1 μm) measurements in 3D elasticity

	Actual	Estimate
Modulus of Elasticity, E	206.85 GPa	199.42 GPa
Shear Modulus, G	80.8 GPa	77 GPa
Poisson's ratio, ν	0.28	0.29

Once again the amount of noise is increased, now to ± 10 μm, and the system is decomposed via POD. The resulting deformations are found in Figure 51.
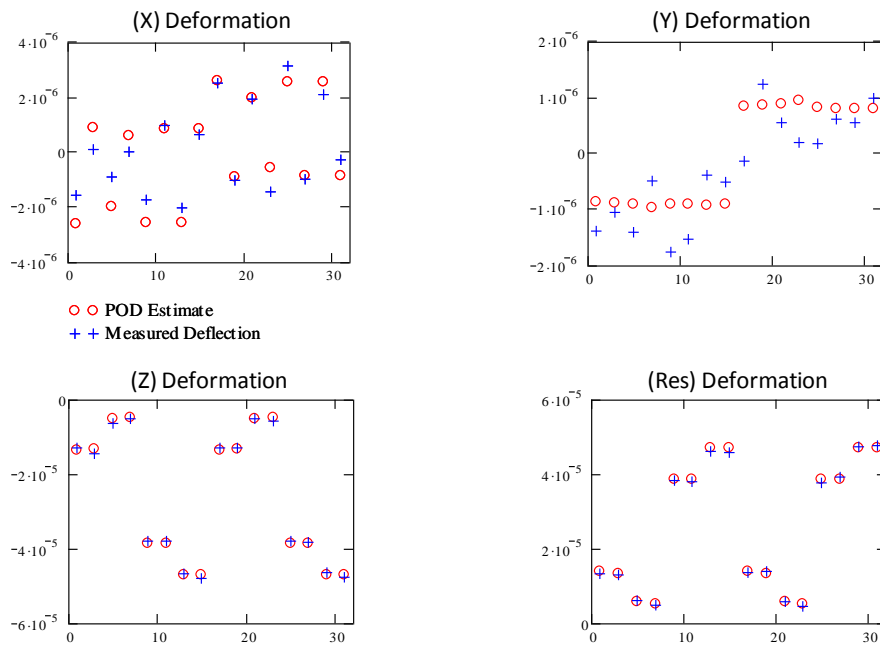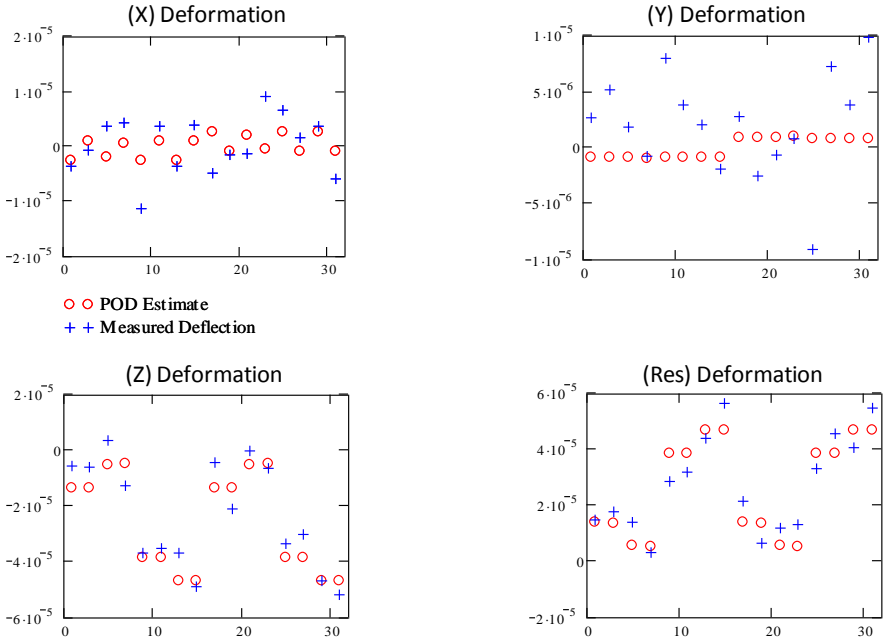

Figure 51 - Comparison of the POD-RBF approximation against the noisy data (± 10 μm) in each

Cartesian direction for 3D elasticity

The resulting material constants can now be seen in Table 16 and are still found with relative accuracy and efficiency. In fact, this example with the larger noise produced more accurate results than the smaller noise approximation. However, this could be attributed to the random distribution of data added to the FEM solution.

Table 16 - Comparison of Actual and POD-RBF estimation of material parameters for noisy data (± 10 μm) measurements in 3D elasticity

	Actual	Estimate
Modulus of Elasticity, E	206.85 GPa	205.59 GPa
Shear Modulus, G	80.8 GPa	78.37 GPa
Poisson's ratio, v	0.28	0.31

Nevertheless for the problem at hand was still able to produce accurate estimations of the material parameters even in the presence of large amounts of noise as seen in both section 4.2.1 and 4.2.2.

4.3 - Fracture Mechanics

For the application to fracture mechanics, a compact tension C(T) specimen has been modeled using FEM software and the above POD-RBF inverse approach is applied to determine the unknown crack length of the C(T) specimen. The C(T) specimen modeled follows ASTM E399 standards for plain strain fracture toughness [15] and can be seen in Figure 52.
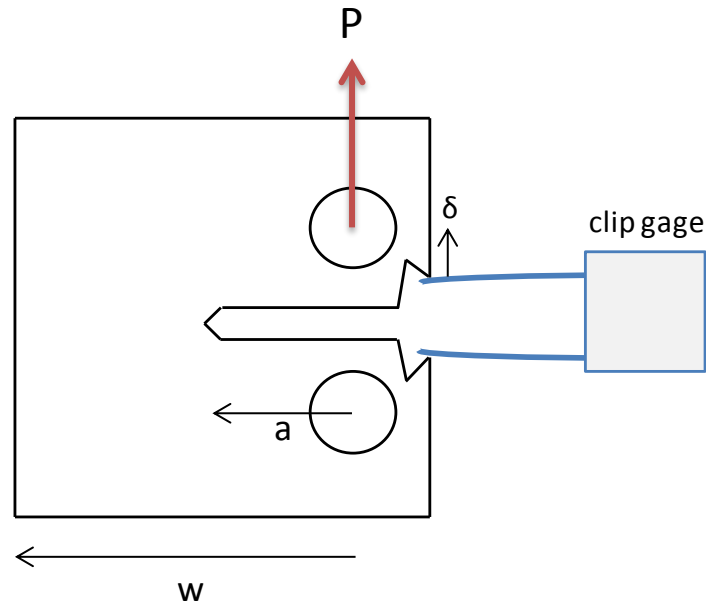
Figure 52 - Model of compact tension specimen

The snapshots were generated by measuring the deformations at the notch opening of the C(T) specimen as to replicate a standard fracture experiment with a clip gage. Various crack length sizes were then implemented via FEM that ranged from 0.35 to 0.55 in. to create the snapshot matrix $\mathbf{U}$, with a total of 21 snapshots M created. Next, the eigenvalues of the covariance matrix $\mathbf{C}$ were calculated and truncated after the 5th eigenvalue of a possible 21, as shown in Table 17.

Table 17 - Table of truncated eigenvalues of fracture mechanics application

λ
2.168×10^8
18.05
3.23
3.21
1.25

The experimental data was then attained from the FEM software using an actual crack length of

0.416 in. No noise was initially added to the FEM solution in order to verify the procedure. The

POD-RBF problem was then solved and returned an approximate value of the crack length equal

to *0.4162 in.* or an error of 0.045%. Although, not discussed in this section for further

redundancy, the regularization parameter was chosen as *α = 0.001* for this problem. A plot of the

deformation and error can be seen in Figure 53.
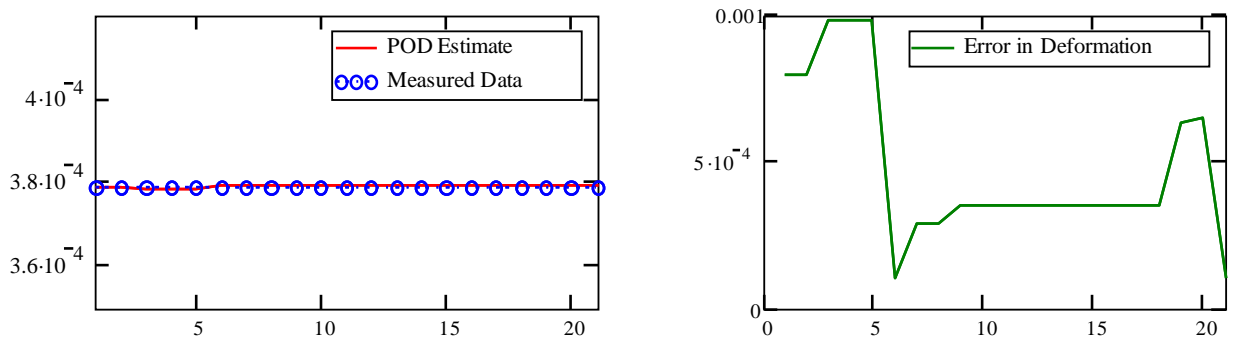
Figure 53 – Deformation (left) and error (right) in no noise solution for fracture problem

As done previously, the problem was then repeated now with noise added to the FEM

solution to mimic empirical data and instrumental error. A normal distribution error of ± 1 μm

was added to the FEM solution using the same crack size, *0.416 in.* The POD-RBF process was

repeated to return a crack length estimate of *0.4161 in.* or an error of 0.035%. The corresponding

plot of the deformation and error can be seen in Figure 54.
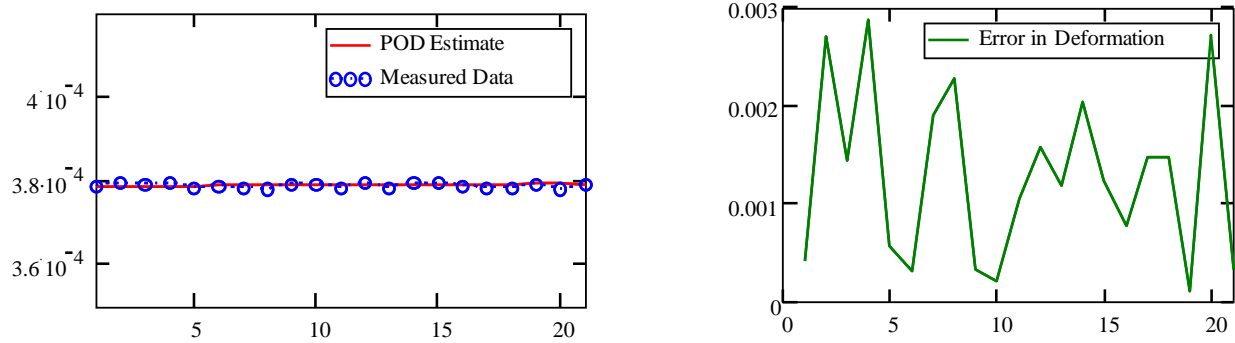
Figure 54 – Deformation (left) and error (right) in ±1 µm noise solution for fracture problem

Additionally, the problem repeated another time with a much larger instrumentation error

added to the solution. A normal distribution noise of ± 10 µm was added using the same crack

length dimension as before. Reapplying the POD-RBF technique provided an approximate value

of the crack length equal to *0.4163 in.* or an error of 0.071%. The results can be seen in Figure

55.
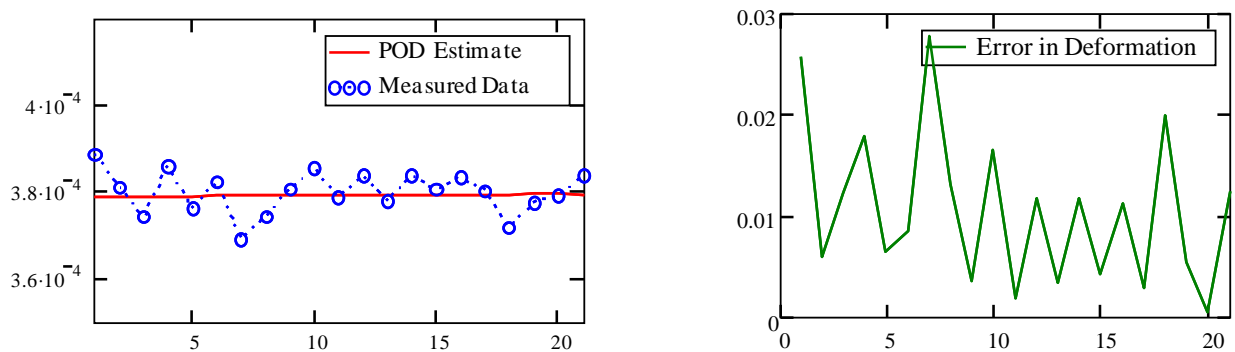
Figure 55 – Deformation (left) and error (right) in ±10 µm noise solution for fracture problem

Observing the deformations presented in Figure 53 - Figure 55, it is easy to see the least squares fit goes through the mean of data, despite the noisy solutions. This allows the POD-RBF inverse routine to optimally pick the crack length with minimal error from the data with regards to the initial snapshot matrix developed. It should also be noted that the deformation error presented in in these figures increases with respect to larger error added into the system. This is not due to a poor estimation of the deformation, but is instead due to the least squares fit capturing the mean of data to present a smooth curved solution.

CHAPTER 5 – CONCLUSIONS

The POD-RBF inverse technique applied in this thesis provided an excellent approach to approximate any unknown parameter to be identified. In the examples outlined, the material parameters or dimensional characteristics determined produced relatively small amounts of error despite the size of the noise attributed to empirical data. This helps to show that the POD inverse technique outlined is quite insensitive to measurement errors, even in the present in somewhat unlikely conditions as shown in the $\pm$ 100 μm elasticity example. Additionally, it takes only a few eigenvalues from the initial snapshot matrices to estimate the desired material parameters and return the temperatures or deformations for the problem at hand.

This technique provides an efficient means of reducing the size and degrees of freedom of the problem while also optimizing accuracy of the solution to be determined. With the addition of a regularization parameter presented inside the LM method, the solution converges effortlessly and quickly.

Although, this thesis only provides examples in regards to certain engineering applications, the overall purpose is to show the reader that the POD-RBF technique can easily be applied to much more complicated systems and domains, as well as to other fields of research. Ideally, these applications can be further proven with realistic experiments in their fields. Nevertheless, the POD-RBF inverse approach provides an inexpensive and nondestructive method to efficiently determine the numerous material parameters under different operating conditions with minimal knowledge of the system at whole.

APPENDIX

Shown below is a direct comparison of the POD methods mentioned throughout this thesis. These methods were proved in more detail from Liang [10] but are taken as an excerpt from [9]. A direct relation from POD to the method of SVD can be stated as

$$\phi = S \tag{55}$$

where the snapshot matrix **U** is written as

$$U = S\Sigma D^T \tag{56}$$

and the amplitude **A** can be shown as

$$A = \Sigma D^T \tag{57}$$

such that the decomposition can be shown equivalent to

$$U = \phi A \tag{58}$$

Karhunen-Loéve Decomposition

The covariance matrix **Q** is defined as

$$Q = UU^T \tag{59}$$

In which the eigenvalues and eigenvectors can be calculated from the nontrivial solution to an eigenvalue problem

$$QL = L\Lambda \tag{60}$$

Where Λ and **L** represent the eigenvalues and eigenvectors of **Q** respectively. Of course, the basis functions are set equivalent to the eigenvectors **L**

$$\phi = L \tag{61}$$

So that **A** from (58) can be calculated using the basis' matrix property of orthogonality

$$A = \phi^T U \tag{62}$$

Transposing the snapshot matrix **U** in (56) becomes

$$U^T = D\Sigma^T S^T \tag{63}$$

where the property of matrix transposition is seen as

$$(XY)^T = Y^T X^T \tag{64}$$

Now substituting (63) and (56) into (59) and utilizing the orthogonality condition of **D** creates

$$Q = UU^T = S\Sigma\Sigma^T S^T \tag{65}$$

Multiplying (65) by **S** and further using its orthogonality property generates

$$QS = S\Sigma\Sigma^T \tag{66}$$

Comparing (66) and (60) one can show that the eigenvectors **L** are said to be equivalent to the left singular vector matrix **S**

$$L = S \tag{67}$$

and the eigenvectors Λ can be denoted as the square of the singular values $\Sigma\Sigma^T$

$$\Lambda = \Sigma\Sigma^T \tag{68}$$

Of course the amplitude matrix **A** is found by multiplying (56) by $\mathbf{S}^T$

$$S^T U = \Sigma D^T \tag{69}$$

And knowing (55) and further comparing (69), (62) and (57); it can be concluded that **A** is equivalent in KLD and SVD.

$$A = \phi^T U = \Sigma D^T \tag{70}$$

73

Principal Component Analysis

In PCA the orthogonal basis functions were determined to be

$$\phi = UV\Sigma^{-1} \tag{71}$$

where Σ represents the matrix of singular values (via SVD) of U and V is the matrix of eigenvectors of the covariance matrix C.

$$C = U^T U \tag{72}$$

So that an eigenvalue problem can be stated as

$$CV = V\Lambda \tag{73}$$

and singular values in matrix Σ are calculated from the eigenvalues Λ such that

$$\sigma_i = \sqrt{\lambda_i} \tag{74}$$

Substituting the eigenvectors V and eigenvalues Λ into (71) the basis functions ϕ can be determined. The amplitudes A can then be computed by first substituting (56) and (63) into (72)

$$C = U^T U = D\Sigma^T \Sigma D^T \tag{75}$$

where the left singular vector matrix S can be removed from orthogonality. Multiplying by D and further using orthogonality

$$CD = D\Sigma^T \Sigma \tag{76}$$

In which (76) can be directly compared to the general eigenvalue problem shown in (73). It can be seen that the right singular vector matrix D is equivalent to the matrix of eigenvectors V of the covariance matrix C

$$V = D \tag{77}$$

and the squares of the singular values $\Sigma^T \Sigma$ are equal to the eigenvalues Λ

$$\Lambda = \Sigma^T \Sigma \tag{78}$$

Now substituting (56) into (71) and replacing **V** with **D** the basis vectors are shown as

$$\phi = S\Sigma D^T D\Sigma^{-1} \tag{79}$$

Utilizing the orthogonality of D, (79) can be reduced to

$$\phi = S\Sigma\Sigma^{-1} \tag{80}$$

such that the basis vectors can be rewritten as

$$\phi = S \tag{81}$$

Of course the amplitudes **A** can be found using (62) and transposing (71) to yield

$$\phi^T = \left(\Sigma^{-1}\right)^T V^T U^T \tag{82}$$

Substituting (82) into (62) and replacing **V** with **D** produces

$$A = \left(\Sigma^{-1}\right)^T D^T U^T U \tag{83}$$

Replacing **U**^{T}**U** with (75) gives

$$A = \left(\Sigma^{-1}\right)^T D^T D\Sigma^T \Sigma D^T \tag{84}$$

and is further reduced via orthogonality

$$A = \left(\Sigma^{-1}\right)^T \Sigma^T \Sigma D^T \tag{85}$$

The property of matrix transposition states

$$\left(X^{-1}\right)^T = \left(X^T\right)^{-1} \tag{86}$$

To simplify (85) as

$$A = \Sigma D^T \tag{87}$$

which shows the amplitude matrix **A** is equivalent to both KLD and SVD methods.

LIST OF REFERENCES

[1] Baeriswyl, P. A., & Rebetez, M. (1997). Regionalization of Precipitation in Switzerland by Means of Principal Component Analysis. *Theoretical and Applied Climatology, 58*, 31-41.

[2] Bialecki, R. A., Kassab, A. J., & Fic, A. (2004). Proper Orthogonal Decomposition and Modal Analysis for Acceleration of Transient FEM Thermal Analysis. *International Journal for Numerical Methods in Engineering, 62*, 774-797.

[3] Breuer, K. S., & Sirovich, L. (1990). The Use of Karhunen-Loeve Procedure for the Calculation of Linear Eigenfunctions. *Journal of Computational Physics, 96*, 277-296.

[4] Chatterjee, A. (2000). An introduction to the proper orthogonal decomposition. *Current Science, 78*(7), 808-817.

[5] Divo, E. A., & Kassab, A. J. (n.d.). *Boundary Element Method for Anisotropic Heterogeneous Heat Conduction.*

[6] Everson, R., & Sirovich, L. (1994). The Karhunen-Loeve Procedure for Gappy Data.

[7] Fic, A., Bialecki, R. A., & Kassab, A. J. (2005). Solving Transient Nonlinear Heat Conduction Problems by Proper Orthogonal Decomposition and the Finite-Element Methods. *Numerical Heat Transfer, 48*, 103-124.

[8] Kerschen, G., Golinval, J.-C., Vakakis, A. F., & Bergman, L. A. (2005). The Method of Proper Orthogonal Decomposition for Dynamical Characterization and Order Reduction of Mechanical Systems: An Overview. *Nonlinear Dynamics, 41*, 147-169.

[9]   Klimaneck, A. (2009). *Numerical Modeling of Heat, Mass and Momentum Transfer in Natural Draft Wet Cooling Tower.* Glewice: Silesian University of Technology. Ph. D. Thesis.

[10] Liang, Y. C., Lee, H. P., Lim, S. P., Lin, W. Z., Lee, K. H., & Wu, C. G. (2002). Proper Orthogonal Decomposition and its Applications - Part 1: Theory. *Journal of Sound and Vibration, 252*(3), 527-544.

[11] Ostrowski, Z., Bialecki, R. A., & Kassab, A. J. (2005). Estimation of Constant Thermal Conductivity by Use of Proper Orthogonal Decomposition. *Computational Mechanics, 37*, 52-59.

[12] Ostrowski, Z., Klimaneck, A., & Bialecki, R. A. (2010). CFD Two-Scale Model of a Wet Natural Draft Cooling Tower. *Numerical Heat Transfer, 57*, 119-137.

[13] Pearson, K. (1901). Of lines and planes of closest fit to system of points in space. *The London, Edinburgh and Dublin Philosophical Magazine and Journal of Science, 2*, 559-572.

[14] Press, W. H., Teukolsky, S. A., Vetterling, W. T., & Flannery, B. P. (1992). *Numerical Recipes in Fortran 77.* New York: Cambridge University Press.

[15] Sanford, R. J. (2003). *Principles of Fracture Mechanics.* Upper Saddle River, NJ: Pearson.

[16] Shlens, J. (2005). *A Tutorial on Principal Component Analysis.* San Diego.

[17] Sirovich, L. (1991). Analysis of turbulent flows by means of the empirical eignefunctions. *Fluid Dynamics Research, 8*, 85-100.

[18] Sirovich, L. (1995). Emprical Eigenfunctions and Low Dimensional Systems. In L. Sirovich, *New Perspective in Turbulence.* Springer-Yerlag.

[19] Stewart, G. W. (1992). *On the Early History of the Singular Value Decomposition.*

[20] Węcel, G., Ostrowski, Z., & Białecki, R. (2010). Proper Orthogonal Decomposition Used to Evaluate Absorption Line Black Body Distribution Function.

[21] Feeney, B. F., & Kappangantu R. J., (1998) On the Physical Interpretation of Proper Orthogonal Modes in Vibrations. *Sound Vibrations, 211*, 607-616.